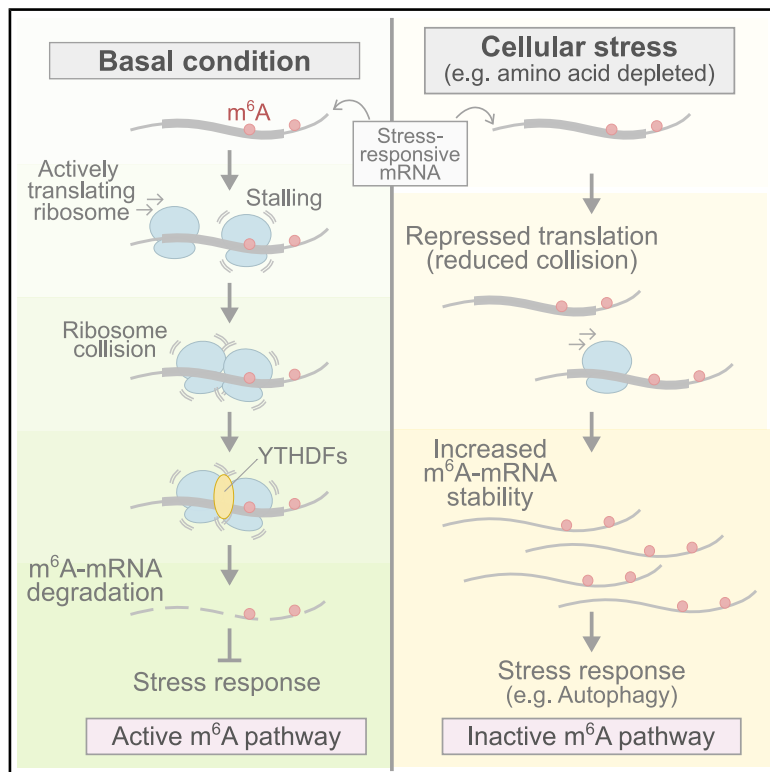


m⁶A alters ribosome dynamics to initiate mRNA degradation

Graphical abstract



Authors

Shino Murakami,
Anthony O. Olarerin-George,
Jianheng Fox Liu, Sara Zaccara,
Ben Hawley, Samie R. Jaffrey

Correspondence

srj2003@med.cornell.edu

In brief

m⁶A is a potent inducer of ribosome stalling and collisions that trigger YTHDF-mediated mRNA degradation, a process that highlights the ribosome as a critical sensor linking translation dynamics to m⁶A-dependent mRNA metabolism.

Highlights

- m⁶A-mRNA degradation is a translation-dependent process
- m⁶A is a potent inducer of ribosome stalling that leads to ribosome collisions
- Ribosome collisions at m⁶A may promote recruitment of YTHDFs for mRNA degradation
- Translation repression during cell stress stabilizes m⁶A-mRNAs for stress responses

Article

m⁶A alters ribosome dynamics to initiate mRNA degradation

Shino Murakami,¹ Anthony O. Olarerin-George,^{1,2} Jianheng Fox Liu,¹ Sara Zaccara,^{1,3} Ben Hawley,¹ and Samie R. Jaffrey^{1,4,*}

¹Department of Pharmacology, Weill Cornell Medicine, Cornell University, New York, NY 10065, USA

²Department of Pharmacology, Physiology & Neuroscience, Rutgers, the State University of New Jersey, Newark, NJ 07103, USA

³Department of Systems Biology, Columbia University, New York, NY 10032, USA

⁴Lead contact

*Correspondence: srj2003@med.cornell.edu

<https://doi.org/10.1016/j.cell.2025.04.020>

SUMMARY

Degradation of mRNA containing N⁶-methyladenosine (m⁶A) is essential for cell growth, differentiation, and stress responses. Here, we show that m⁶A markedly alters ribosome dynamics and that these alterations mediate the degradation effect of m⁶A on mRNA. We find that m⁶A is a potent inducer of ribosome stalling, and these stalls lead to ribosome collisions that form a unique conformation unlike those seen in other contexts. We find that the degree of ribosome stalling correlates with m⁶A-mediated mRNA degradation, and increasing the persistence of collided ribosomes correlates with enhanced m⁶A-mediated mRNA degradation. Ribosome stalling and collision at m⁶A is followed by recruitment of YTHDF m⁶A reader proteins to promote mRNA degradation. We show that mechanisms that reduce ribosome stalling and collisions, such as translation suppression during stress, stabilize m⁶A-mRNAs and increase their abundance, enabling stress responses. Overall, our study reveals the ribosome as the initial m⁶A sensor for beginning m⁶A-mRNA degradation.

INTRODUCTION

N⁶-methyladenosine (m⁶A) is a modified nucleotide that is enriched in specific mRNAs and regulates cell growth,¹ differentiation,^{2,3} and cellular stress responses.^{4–7} m⁶A is synthesized on mRNAs by a heterodimeric methyltransferase comprising METTL3 and METTL14.⁸ The major effect of m⁶A is to promote mRNA degradation.^{9,10} Thus, mRNAs with m⁶A are often maintained at low levels. Many of these mRNAs encode critical regulators of key cellular processes, and their upregulation is needed for activating diverse cellular responses.^{2,6,11–15}

The cellular stress response relies on proteins encoded by m⁶A-mRNAs. For example, amino acid depletion stress alters gene expression to enhance conservation of resources, restore nutrient levels, and promote stress resistance.¹⁶ These pathways often utilize m⁶A-enriched transcripts that encode metabolic regulators, DNA-repair pathway proteins, and autophagy proteins^{4,12–15,17–21} (Table S1). Although the levels of some of these mRNAs have been found to increase during stress,^{22–28} it is not known whether these increases are due to suppression of m⁶A-mediated mRNA degradation.

m⁶A-mediated mRNA degradation requires the binding of YTHDF proteins, which recruit mRNA degradation machinery.^{29,30} However, m⁶A also affects ribosome translocation, with numerous studies demonstrating that m⁶A can induce

ribosome stalling,^{31–34} potentially by impairing decoding kinetics.^{31,32} Whether and how m⁶A-induced ribosome stalling contributes to m⁶A-mediated degradation remains unclear.

Here, we show that m⁶A-mRNA degradation is driven by altered ribosome dynamics during translation. m⁶A is a potent inducer of ribosome stalling, with the degree of stalling influenced by the codon context of the m⁶A site. Stronger stalls lead to more effective m⁶A-mediated mRNA degradation. In some cases, m⁶A-induced stalling is so pronounced that it causes ribosome collisions. These collisions may produce unique ribosome footprints with conformations distinct from other types of collided ribosomes. Prolonging ribosome collisions significantly enhances m⁶A-mediated degradation, suggesting that collisions may play a direct role in linking m⁶A-induced stalling to mRNA degradation. Our data further suggest that ribosome stalling and collisions may facilitate the binding of YTHDF m⁶A reader proteins, promoting mRNA degradation. This translation-dependent m⁶A-mRNA degradation pathway is suppressed when translation is reduced, such as during cell stress. This leads to the stabilization of m⁶A-mRNAs and increases the expression of stress-response transcripts. Thus, the ribosome acts as the initial m⁶A sensor, triggering stalling, collisions, and YTHDF-mediated degradation. This pathway explains the low basal expression of m⁶A-mRNAs and their increased expression during cellular stress.

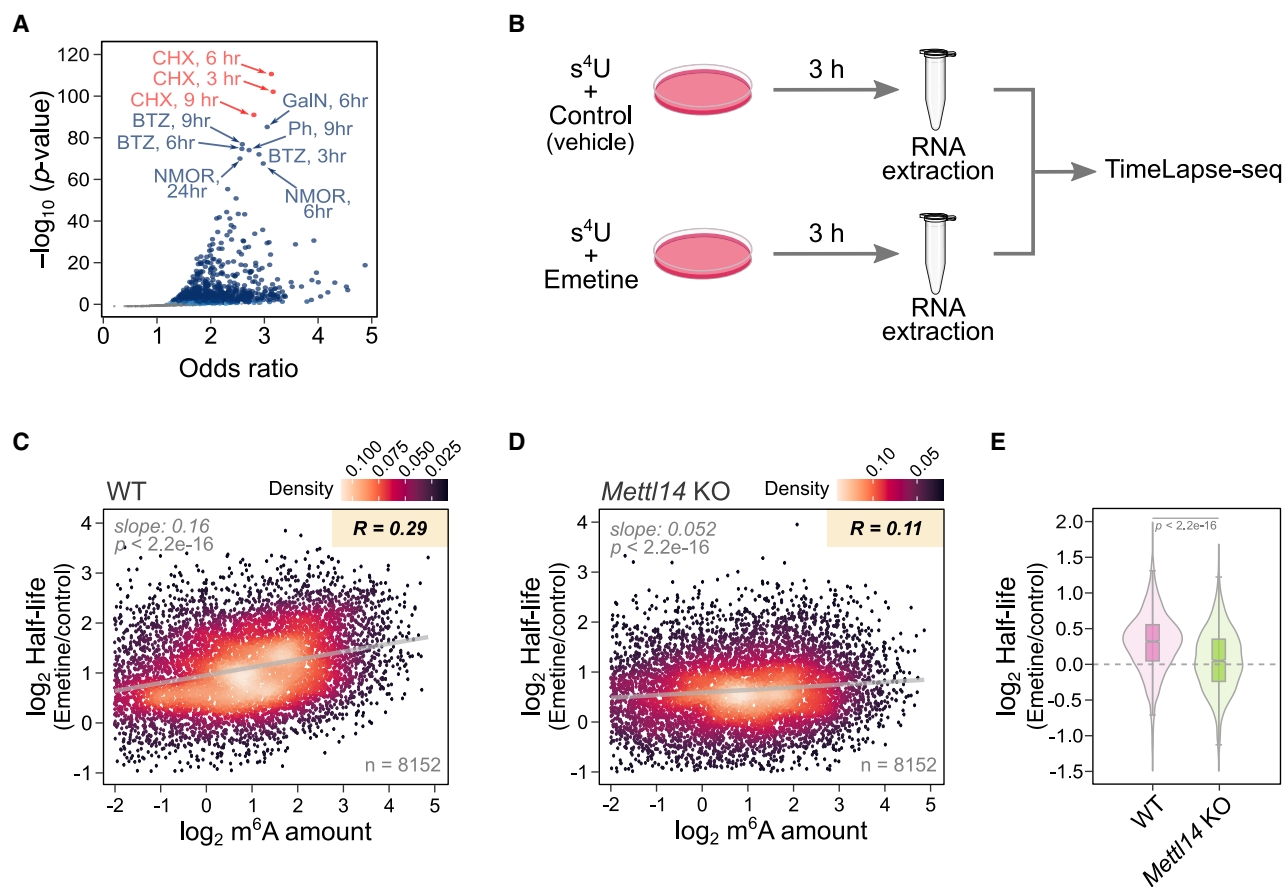


Figure 1. m⁶A-mRNA degradation is a translation-dependent process

(A) Cycloheximide exhibits the most significant coordinated increase in expression of highly methylated m⁶A-mRNA among 170 different pharmacologic treatments. Cycloheximide was the only translation inhibitor in the screen. CHX, cycloheximide; GalN, galactosamine; BTZ, bortezomib; Ph, phoron; NMOR, N-nitrosomorpholin. Darker to lighter blue dots, the most to least significant treatments (*p* value < 0.05); gray dots, non-significant treatments; red dots, top three most significant treatments.

(B) Schematic of the TimeLapse-seq experiment. 4sU, 4-thiouridine. *n* = 3 biological replicates.

(C) Change in mRNA half-life of each transcript after emetine treatment in mESC was plotted against the cumulative m⁶A amount.³⁷ The stabilization effect of emetine correlates with the m⁶A amount.

(D) Emetine-induced mRNA stabilization in Mettl14 knockout mESC.

(E) To determine whether m⁶A-mRNAs are a major target of translation-mediated mRNA degradation, we measured emetine-induced increases in mRNA half-life throughout the transcriptome in wild-type (pink) and in Mettl14 knockout mESC (green). The median mRNA stabilization of emetine was markedly reduced in Mettl14 mESC compared with wild-type cells. Two-sided Wilcoxon signed-rank test. Boxplots show the median, upper/lower quartiles, and whiskers at 1.5× interquartile ranges.

See also Figure S1.

RESULTS

m⁶A-mRNA degradation is a translation-dependent process

Although a major function of m⁶A is to promote mRNA degradation, it remains unclear whether and how m⁶A-mediated degradation might be regulated. We screened the Toxicogenomic Project consortium database, which contains gene expression analysis from cells that were treated with 170 bioactive compounds.³⁵ We asked whether any treatment is associated with increased expression of highly methylated mRNAs. We used a list of 1,780 genes containing >5 m⁶A sites based on miCLIP, a method for transcriptome-wide m⁶A map-

ping.³⁶ Among all the treatments, the translation inhibitor cycloheximide exhibited the most significant increase in expression of highly methylated genes compared with the remaining cellular transcripts (Figure 1A; Table S2). These data suggested that m⁶A-mRNA degradation is linked to mRNA translation.

To find additional regulators of m⁶A-mRNA degradation, we examined the Cancer Dependency Map (DepMap), which can be used to discover genes in functionally related cellular pathways.^{38–40} As expected, the top genes functionally relevant to METTL3 included known m⁶A pathway genes such as METTL14 and YTHDF2. However, among the top 100 genes, 30 were related to mRNA translation (Figure S1A; Table S3).

To test whether translation is required for m⁶A-mRNA degradation, we measured mRNA half-lives after translational inhibition with emetine in mouse embryonic stem cells (mESCs) using TimeLapse-seq (Figures 1B and S1B). Here, we saw a strong correlation between m⁶A levels per transcript and emetine-induced mRNA stabilization (Figure 1C).

We next examined *Mettl14* knockout mESC, which lack nearly all m⁶A in mRNA.² In *Mettl14* knockout mESC, the stabilizing effect of emetine was reduced in mRNAs that are normally highly methylated (Figures 1D and S1C–S1E). Thus, the stabilizing effect of emetine is mostly dependent on the presence of m⁶A.

Using a previously published dataset of gene expression after translation inhibition with puromycin,⁴¹ we again saw a clear relationship between the m⁶A level in mRNA and increased mRNA expression after translational inhibition (Figure S1F).

In contrast to m⁶A levels, transcript length and coding sequence length showed low to no correlation with emetine-induced mRNA stabilization (Figures S1G and S1H).

It is well known that translation inhibition results in a transcriptome-wide stabilization of mRNAs.^{42,43} Indeed, in wild-type mESC treated with emetine, we found a median fold-increase in mRNA half-life of 0.32 (Figure 1E). However, the global emetine-induced mRNA stabilization effect dropped to 0.05 in *Mettl14* knockout mESC (Figure 1E). Thus, translation-dependent mRNA degradation is largely due to m⁶A.

We wanted to determine whether some m⁶A-mRNAs are degraded in a translation-independent manner. We therefore compared the change in mRNA half-lives induced by m⁶A depletion with the change in mRNA half-lives after emetine treatment (Figure S1I). The overall pattern of half-life changes was similar; however, emetine often exhibited a stronger effect, suggesting that additional mechanisms may also contribute to the general stabilization effect of emetine as seen in Figure 1E.

Overall, our results suggest that m⁶A-mRNAs require translation for their degradation and that this pathway explains much of the previously observed phenomenon of translation-dependent mRNA degradation.

m⁶A induces pronounced ribosome stalls

Our finding that m⁶A-mRNA degradation depends on active translation is in line with the stabilization effect of m⁶A-mRNAs by emetine observed by others in HEK293T cells.³⁴ These effects correlate with enhanced m⁶A-mRNA localization to P-bodies, but a mechanism to explain why the degradation effect of m⁶A is induced by translation was unclear. Additionally, previous studies showed that m⁶A induces subtle ribosome stalling in mouse embryonic fibroblasts (MEFs) and HEK293T cells.^{33,34} However, it was unclear whether and how ribosome stalling at m⁶A sites is linked to mRNA degradation. To explore the effect of m⁶A on ribosome stalling, we re-examined the effect of m⁶A on the ribosome stalling at high-stoichiometry m⁶A sites based on GLORI, a quantitative m⁶A mapping method.³⁷

In this analysis, we mapped ribosome footprints using OTTR ribosome profiling, a recently developed highly sensitive ribosome profiling method.⁴⁴ To determine ribosome stalling, we analyzed ribosome footprints that aligned to mRNA regions with known m⁶A sites. For each m⁶A site, we counted the number of ribosomes with their A-site positioned over the first nucle-

otide of the m⁶A-containing codon. To assess whether ribosome occupancy at these sites was higher than surroundings, we calculated Z scores by comparing ribosome occupancy at each nucleotide position relative to the m⁶A site to the local mean of occupancy for each m⁶A site. This approach provided an internal normalization method, controlling for variations in translation efficiency between transcripts. The stalling index was then defined as the mean Z score at each nucleotide position surrounding m⁶A-containing codons, providing a standardized measure of ribosome stalling.

We found that ribosome stalling at m⁶A sites strongly correlates with m⁶A stoichiometry, with high-stoichiometry (59%–100%) m⁶A sites exhibiting a ~650% increase in stalling compared with adjacent codons (Figures 2A and S2A–S2C). This effect was significantly greater than previously reported (~50%–60% increase for non-methylated control codons³³), likely due to our ability to selectively analyze high-stoichiometry m⁶A sites and the improved sensitivity of OTTR ribosome profiling data.⁴⁴ Moreover, the pronounced ribosome stalling at m⁶A sites was dependent on the presence of m⁶A, as these sites no longer exhibit increased ribosome occupancy in *Mettl14* knockout mESC (Figure S2A). These results indicate that m⁶A-induced ribosome stalling is much more prominent than previously recognized.

m⁶A is limited to the DRACH sequence context (D = A,G,U; R = A,G; H = A,C,U)^{45,46} and thus can only appear in 9 different codons (m⁶ACC, m⁶ACU, m⁶ACA, G-m⁶AC, A-m⁶AC, AG-m⁶A, GA-m⁶A, GG-m⁶A, and AA-m⁶A). We found even higher stalling at m⁶A sites with >90% stoichiometry, especially at some m⁶A codons (e.g., GA-m⁶A and AA-m⁶A) compared with others (Figures 2B, S2D, and S2E).

We next wanted to know whether the degree of m⁶A-induced ribosome stalling is linked to m⁶A-mRNA degradation. We first measured the degradation effect of m⁶A as the impact of each m⁶A-containing codon on m⁶A-mediated mRNA degradation. To do this, we measured mRNA expression changes in HEK293T cells after treatment with STM2457,⁴⁷ a selective METTL3 inhibitor⁴⁸ (Figure S2F). We then measured a correlation coefficient between the cumulative stoichiometry of each of the 9 m⁶A-containing codons and the degree of m⁶A-mediated mRNA degradation throughout the transcriptome, a metric build based on the codon stability coefficient defined by Presnyak et al.⁴⁹ (Figure 2C). As expected, we saw a positive correlation between cumulative m⁶A stoichiometry and m⁶A-mediated mRNA degradation for each codon (correlation is indicated by the position on the y axis of Figure 2C). We then asked whether the ability of each m⁶A codon to induce mRNA degradation was related to its ability to induce stalling. A plot of the degree of stall versus the degradation effect of m⁶A for each codon showed a strong correlation ($R = 0.74$) (Figure 2C). Thus, m⁶A-containing codons that exhibit the most stalling tend to exhibit the most prominent effects on m⁶A-mediated mRNA degradation.

As a control, we examined the corresponding non-methylated codons. For these experiments, we selected codons that were in the DRACH motif but exhibited low m⁶A stoichiometry (i.e., <5%). We then assessed the correlation between the degradation effects and ribosome stalling for these corresponding non-methylated codons. Here, we saw a weak negative

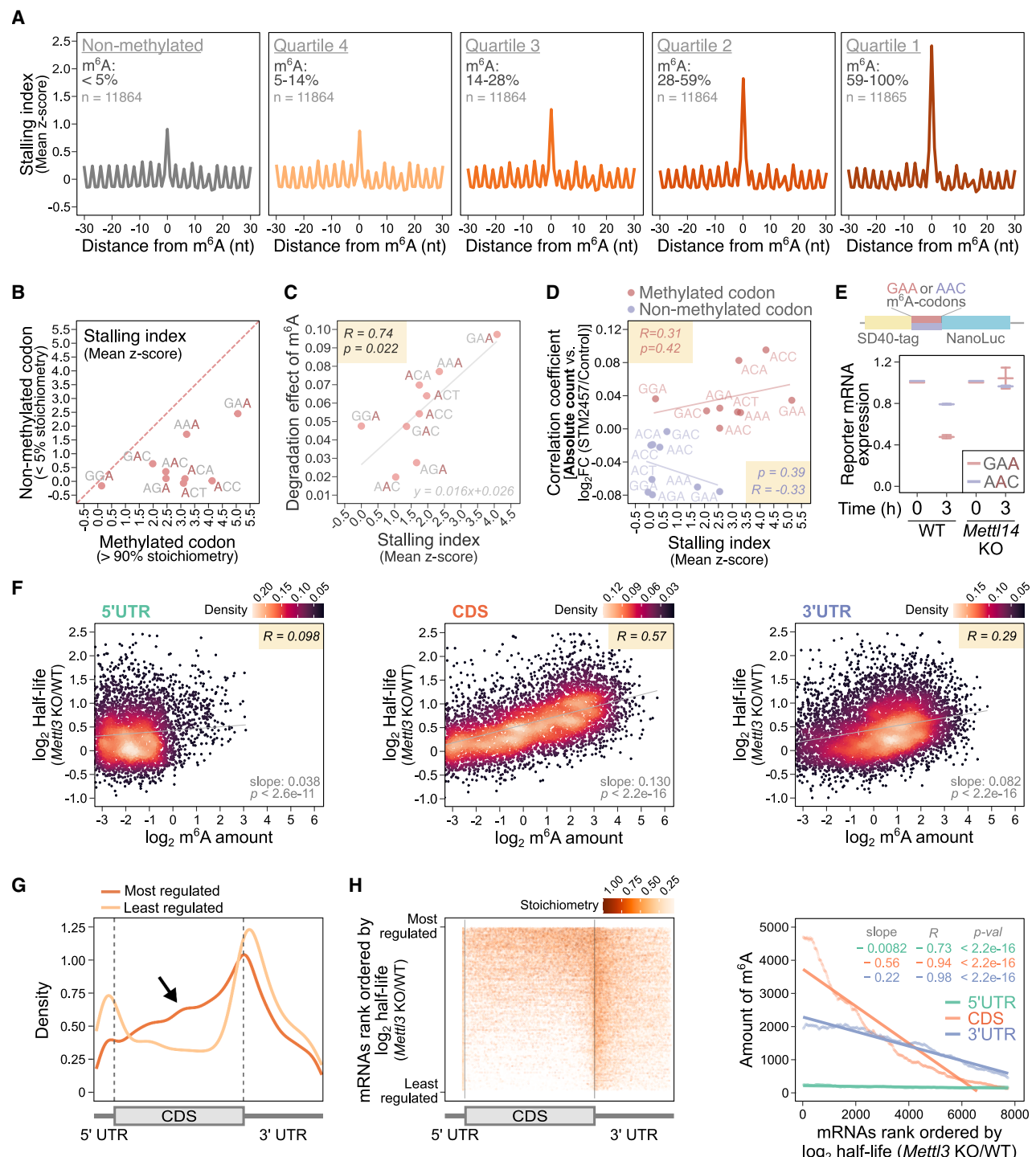


Figure 2. m⁶A-induced ribosome stalling is linked to m⁶A-mRNA degradation

(A) m⁶A in the A-site of the ribosomes induces marked ribosome stalling. Mean Z score of A-site count was plotted relative to the first nucleotide of m⁶A-containing codons. Plots were generated for CDS m⁶A grouped in quartiles based on their stoichiometry. Non-methylated matched codons in DRACH (D = A,G,U; R = A,G; H = A,C,U) motifs was randomly selected from the same set of transcripts to match the number of m⁶A codons in each quartile.

(B) Ribosomes exhibit different degrees of stalling at m⁶A depending on the codon sequence context. Mean Z score of A-site count is plotted for each codon in its methylated ($>90\%$ stoichiometry) and non-methylated ($<5\%$ stoichiometry) state. Methylated adenosine residues within codons are highlighted in red. The non-methylated codons in DRACH motifs were selected from the same set of transcripts that contained the methylated codons.

(legend continued on next page)

correlation between stalling at the non-methylated codons and their degradation effects (Figures 2D and S2G). This suggests that m⁶A, and not the codon sequence itself, accounts for the degradation effect of the methylated codons.

To further test the role of ribosome stalling, we created reporter transcripts that contain a coding sequence with internal clusters of GAA*CU motifs, which is associated with highly efficient methylation of the second adenine (indicated with asterisk). Notably, GA-m⁶A causes relatively high stalling while A-m⁶AC causes low stalling (see Figure 2C). We therefore adjusted the reading frame of the reporter so that the m⁶A was located in the GAA* codon in one reporter, while m⁶A was located in AA*C codons in the other reporter. The remainder of the reporter was designed to lack m⁶A consensus motifs.

When we measured the stability of these reporter mRNAs, the reporter for the stalling-prone GA-m⁶A codon was more unstable compared with the reporter containing the A-m⁶AC codon, which induces weaker stalling (Figure 2E). The destabilization effects of these codons were mediated by m⁶A since both reporters were highly stabilized in *Mettl14* knockout mESC.

Taken together, these results suggest that m⁶A-induced ribosome stalling leads to m⁶A-mediated mRNA degradation.

m⁶A sites encountered by the ribosome promote mRNA degradation

To further test the role of m⁶A-induced ribosome stalling, we asked whether m⁶A sites in the 3' UTR contribute to m⁶A-mediated mRNA degradation. 3' UTR m⁶A sites do not encounter the ribosome and thus do not induce stalls. We defined m⁶A-mediated mRNA degradation by comparing mRNA half-lives in wild-type cells with m⁶A-deficient cells. In this analysis, there was a strong correlation between the coding sequence (CDS) m⁶A levels and m⁶A-mediated mRNA degradation ($R = 0.57$) (Figures 2F and S3A). However, the correlation was markedly reduced with 3' UTR m⁶A ($R = 0.29$). There was minimal correlation with 5' UTR m⁶A ($R = 0.098$). Notably, when we plotted the m⁶A metagene for mRNAs that undergo high m⁶A-mediated

degradation compared with low m⁶A-mediated degradation, we could see a clear enrichment of m⁶A in the CDS for those mRNAs with high m⁶A-mediated degradation (Figures 2G and S3C).

We next visualized how the location of m⁶A in the transcript body correlates with m⁶A-mediated mRNA degradation. mRNAs were ranked based on the level of m⁶A-mediated degradation in MEFs. Each m⁶A site was plotted as a circle that was color-coded based on the stoichiometry. As expected, transcripts with the highest m⁶A-mediated degradation had the most m⁶A (Figure 2H). However, it was also clear that m⁶A-mediated degradation was more closely correlated with m⁶A levels in the CDS rather than the 3' UTR (Figures 2H and S3B). Overall, these data suggest that the m⁶A sites encountered by the ribosome have a more prominent effect on mRNA degradation, compared with 3' UTR m⁶A sites that do not encounter the ribosome.

To test whether the mRNA stabilization effect of emetine is mediated by CDS m⁶A, we re-examined the ability of emetine to stabilize m⁶A-mRNAs (see Figures 1C and 1D) by grouping mRNA based on their m⁶A levels in the 5' UTR, CDS, or 3' UTR. Using this approach, CDS m⁶A levels were more strongly linked to emetine-induced mRNA stabilization (Figures S3D and S3E).

To determine the contribution of m⁶A in the 3' UTR to m⁶A-mRNA degradation, we examined genes that have m⁶A only in CDS or only in 3' UTR. We found even greater difference between CDS m⁶A and 3' UTR m⁶A on mRNA half-life (Figures S3F-S3I). We then compared mRNAs that only contain CDS m⁶A with mRNAs with both CDS m⁶A and 3' UTR m⁶A. When these mRNAs were compared based only on the amount of CDS m⁶A, the presence of additional 3' UTR m⁶A sites did not substantially increase m⁶A-dependent mRNA degradation except when CDS m⁶A levels were low (Figures S3J-S3L). In contrast, when we examined mRNAs based on 3' UTR m⁶A amount, the presence of additional CDS m⁶A substantially increased m⁶A-dependent degradation (Figures S3K and S3L).

We also examined two reporter mRNAs derived from endogenous genes that contain m⁶A in their coding sequence and undergo m⁶A-mediated mRNA degradation. Both reporters were

(C) m⁶A-induced ribosome stalling is linked to m⁶A-mediated mRNA degradation. The degradation effect of m⁶A for each m⁶A-containing codon was calculated as a Pearson correlation coefficient between cumulative m⁶A stoichiometry for each mRNA and the degree of m⁶A-mediated mRNA degradation. We then plotted the degradation effect of m⁶A against the stalling index for each m⁶A-containing codon. Methylated adenosine residues within codons are highlighted in red. Pearson correlation.

(D) Ribosome stalling at non-methylated codons show general anti-correlation to m⁶A-mediated mRNA degradation. The Pearson correlation coefficients between the absolute number of non-methylated codons and the degree of m⁶A-mediated mRNA degradation were calculated. Each correlation coefficient was plotted against ribosome stalling index at each codon in purple. Correlation for corresponding methylated codons is shown in red. Pearson correlation.

(E) Comparison of stalling-prone GA-m⁶A-codon with less stalling A-m⁶AC-codon. (Top) Schematic of the reporters. (Bottom) Stability of reporters was measured using actinomycin D. The GA-m⁶A reporter was more unstable compared with the A-m⁶AC reporter. Both reporters were similarly stabilized in *Mettl14* knockout mESC. Data shown as mean ± SEM. $n = 3$ biological replicates.

(F) Correlation between 5' UTR, CDS, and 3' UTR m⁶A levels and m⁶A-mediated mRNA degradation. We compared the m⁶A levels in each region of mRNA³⁷ and the degree of m⁶A-dependent degradation for each mRNA. An mRNA's CDS m⁶A levels were most strongly correlated with the mRNA's increase in mRNA half-life in *Mettl3* knockout MEFs. $n = 10,713$ transcripts.

(G) m⁶A metagenes of transcripts that are most (dark orange; top 10%) and least (light orange; bottom 10%) regulated by m⁶A. The mRNAs that undergo the highest degree of m⁶A-mediated degradation show noticeably greater CDS enrichment of m⁶A.

(H) m⁶A that encounters the ribosome most strongly correlates with m⁶A-mRNA instability. (Left) Genes were ranked on the y axis based on their degree of m⁶A-mediated degradation determined as the fold-increase in mRNA half-life in *Mettl3* knockout relative to wild-type MEFs. The relative location of m⁶A in each length-scaled transcript was plotted as a circle colored based on the m⁶A stoichiometry (darker to lighter orange; high to low m⁶A stoichiometry). mRNAs that undergo the highest degree of m⁶A-mediated mRNA degradation show m⁶A all along the CDS and 3' UTR. However, in mRNAs that show minimal m⁶A-mediated mRNA degradation have few CDS m⁶A sites, while m⁶A remains abundant in 3' UTR. (Right) Quantification of m⁶A levels in the 5' UTR, CDS, and 3' UTR in left. See also Figures S2 and S3.

relatively unstable in wild-type mESC and stabilized in *Mettl14* knockout mESC. However, when the ability of the ribosome to encounter m⁶A was blocked by introducing a stop codon prior to the m⁶A sites, or by treating cells with emetine, the reporter transcripts were stabilized (Figure S3M).

Taken together, these data support the idea that the ribosome is needed for m⁶A-mediated mRNA degradation since m⁶A sites encountered by the ribosome have a more prominent effect on m⁶A-mediated degradation. However, 3' UTR m⁶A may contribute to degradation since these sites make a small but detectable contribution to m⁶A-mediated mRNA degradation.

m⁶A induces ribosome collisions

Because ribosomes exhibit such prolonged stalls at m⁶A, these ribosomes may be prone to undergoing ribosome collisions. To test this, we set up an *in vitro* assay to measure ribosome collisions. We incubated [³²P]-labeled mRNA with translationally active HeLa lysates and generated ribosome footprints using micrococcal nuclease. We prepared a standard for disome footprints using a low concentration of emetine (0.5 μM), which induces sporadic ribosome arrests and subsequent ribosome collisions.^{50,51} A monosome standard was prepared using high-dose emetine (200 μM), which fully blocks ribosome translocation and thus prevents collisions.^{50,51} The monosome and disome standards were readily distinguished using gel electrophoresis ³²P-imaging (Figure 3A).

We then asked whether m⁶A induces ribosome collisions. mRNA lacking m⁶A generated only monosomes (Figures 3A, bottom right and S4A), however, m⁶A-containing mRNA lead to an increase in both the monosomes and disomes, and potentially trisomes (Figure 3A, bottom right and S4A). Importantly, ribosome footprints were nearly absent unless translation was initiated by eIF4E. Overall, these results suggest that translating ribosomes stall at m⁶A, which triggers ribosome collisions.

Global mapping of disomes reveals ribosome collisions at m⁶A in cells

Next, we tested whether m⁶A promotes ribosome collisions in cells. We mapped the 5' and 3' extremities of disome footprints and plotted them relative to the first nucleotide of m⁶A-containing codons. We found a clear enrichment of disome fragments around m⁶A (Figures 3B and S4B). In contrast, when we mapped disome footprints around sequence-matched non-methylated codons, we found no significant enrichment (Figure S4B). These data suggest that disomes are selectively enriched around m⁶A.

We also examined an earlier map of ~2,000 collided disomes across HEK293 cells.⁵² Although this study had many fewer disomes than OTTR ribosome profiling, we found that disomes were substantially more likely to derive from m⁶A-mRNAs than mRNAs lacking m⁶A (Figures S4C-S4E).

To further test whether ribosome collisions on m⁶A-mRNA depends on m⁶A, we quantified disomes in wild-type and *Mettl3* knockout MEFs. We prepared lysates from these cells and subjected them to partial digestion with RNaseA to isolate monosomes and disomes.⁵¹ The amount of disomes in *Mettl3* knockout cells decreased by ~40% compared with the wild-type cells (Figure 3C). However, monosomes were decreased by only ~15% in *Mettl3* knockout cells compared with the

wild-type cells. Together, these data suggests that m⁶A is a source of ribosome collisions in cells.

m⁶A-induced collided ribosomes exhibit a unique conformation

The conformations of stalled and collided ribosomes are reflected by different footprint lengths and positions relative to stalling features.^{44,53,54} For example, “true disomes” are seen at stop codons in HEK293T cells, which correspond to footprints whose 5' and 3' extremities are located at 44–48 nt upstream and 14–21 nt downstream of the stop codon.⁴⁴ We observed a similar pattern of true disomes around stop codons in our analysis of footprints in HEK293T cells (Figure 3B).

We next examined disomes formed at m⁶A sites.⁴⁴ The disome footprints have a 5' extremity that is ~44–48 nt upstream of the m⁶A-containing A-site, which corresponds the position of the lagging collided ribosome in a true disome. However, the leading stalled ribosome exhibited an altered conformation since the 3' extremity of the disome footprint was only 4–8 nt downstream of the m⁶A-containing A-site (Figure 3B). This truncation at the 3' extremity is distinct from 3' extremity of disomes at stop codons⁴⁴ (Figure 3B). Thus, ribosome collisions at m⁶A may induce a distinct conformational state of the stalled ribosome. Conceivably, the unique conformation of the m⁶A-induced disome may enable the induction of m⁶A-dependent mRNA degradation.

Notably, the 3' extremity of the disome footprint at m⁶A sites is different from the 3' extremity of stalled monosome footprints at m⁶A (Figure 3D). Stalled monosomes produce a footprint whose 3' extremity is at the expected 16–20 nt downstream of the A-site.⁴⁴ Thus, the initial stalling leads to a more conventional conformation but subsequent collision possibly affects the leading ribosome's conformation.

Increasing collided ribosomes promotes m⁶A-mRNA degradation

To test the role of ribosome collisions in m⁶A-dependent mRNA degradation, we examined the effect of increasing the persistence of collided ribosomes. A key downstream event in response to ribosome collisions is recruitment of disassembly factors, including the ASC-1 helicase complex that disassembles the leading stalled ribosome in disomes.⁵⁵ As a result, depletion of ASCC3 (a helicase subunit of the ASC-1 complex) leads to an increase in the persistence of collided ribosomes.⁵⁵ We therefore examined gene expression changes associated with ASCC3 depletion.⁵⁶ Compared with mock small interfering RNA (siRNA)-treated cells, ASCC3-depleted cells exhibited enhanced m⁶A-mediated mRNA degradation (Figures 3E and S4F).

These results suggest that ribosome stalling and subsequent ribosome collision at m⁶A promotes m⁶A-mRNA degradation.

Altered ribosome dynamics may facilitate YTHDF recruitment to m⁶A

m⁶A-mRNA degradation was previously shown to be mediated by the YTHDF m⁶A reader paralog proteins, YTHDF1, YTHDF2, and YTHDF3,^{10,57} which recruit the mRNA degradation machinery for m⁶A-mRNA degradation.^{29,57} Thus, we asked whether YTHDF-mediated m⁶A-mRNA degradation is distinct from translation-dependent m⁶A-mRNA degradation, or alternatively,

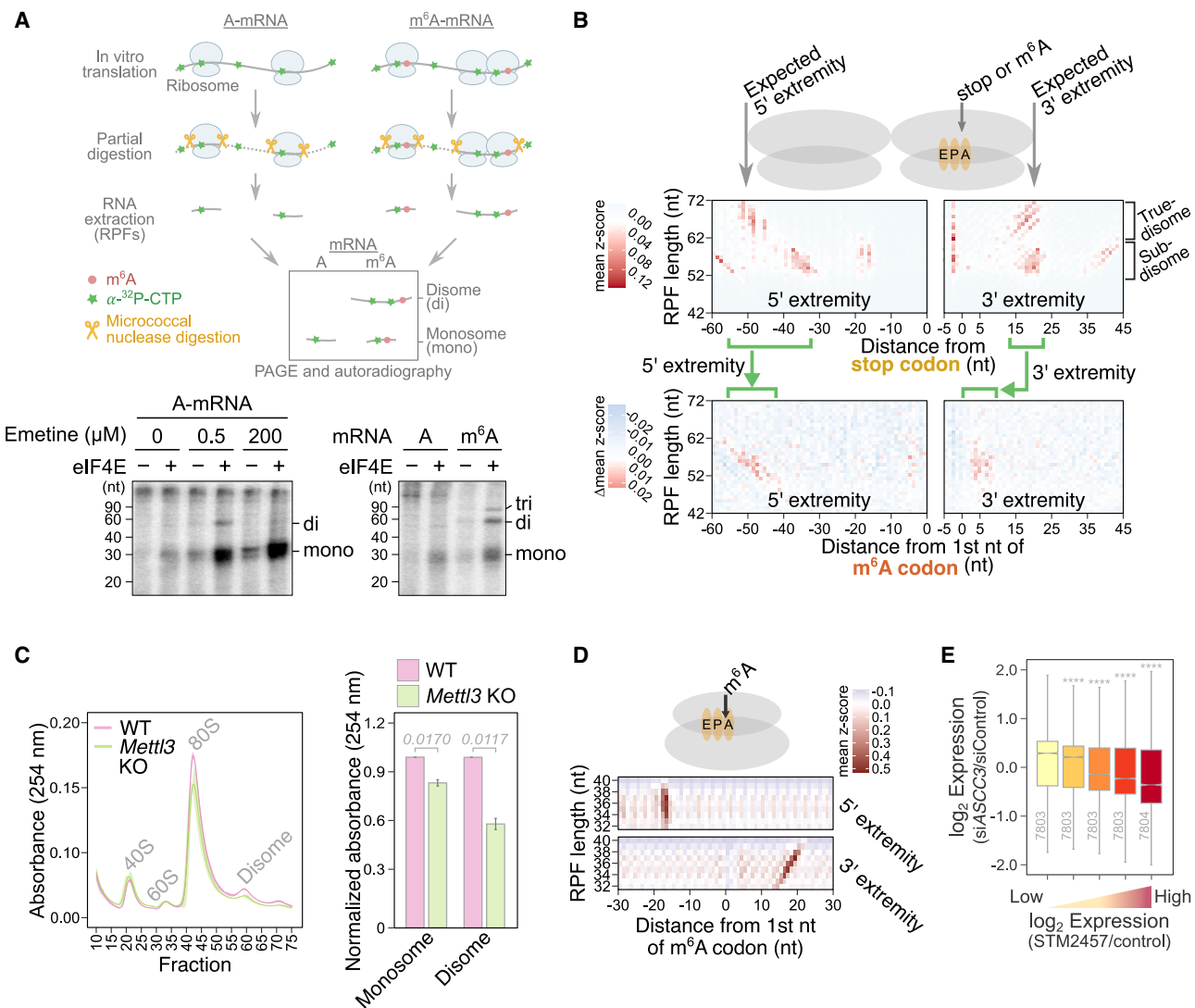


Figure 3. m⁶A induces ribosome collisions with a unique conformation

(A) m⁶A induces ribosome collisions *in vitro*. (Top) Schematic of the *in vitro* disome footprinting assay. (Bottom left) Standards for the mobility of monosome and disome footprints. Ribosome footprints of ~29 and ~58 nt corresponds to monosome and disome footprints. (Bottom right) A- and m⁶A-mRNA generated ~29 nt monosome footprints. Additionally, m⁶A-mRNA generated additional footprints at ~56 nt and ~86 nt, corresponding to disomes and potentially trisomes.

(B) m⁶A induces a novel disome conformation in cells. The 5' and 3' extremities of disome footprints were mapped relative to the stop codon or the m⁶A-containing codons. Background footprints around non-methylated sequence-matched control codons were subtracted from footprints around m⁶A-containing codons. Shown are the background-subtracted mean Z score of the 5' and 3' extremity coverage for each length of disome footprints. The leading stalled ribosome within disomes at m⁶A sites exhibit altered footprints, suggesting that m⁶A-induced collisions lead to a unique conformation of the stalled ribosome.

(C) m⁶A is a source of collided ribosomes in cells. (Left) Traces of ribosome sucrose gradient fractionation. The line and shadow represent the mean and standard deviation, respectively. (Right) Monosomes and disomes in Mettl3 knockout MEFs were quantified relative to the wild type. Data shown as mean ± SEM. Two-sided t test; p values are shown. n = 3 biological replicates.

(D) Monosome footprints in the vicinity of m⁶A. The 5' and 3' extremities of monosome footprints relative to m⁶A-containing codons were visualized for each length of footprints.

(E) To test whether m⁶A-mRNA degradation is mediated by ribosome collisions, we tested the effect of increasing the persistence of ribosome collisions using ASCC3 knockdown. We plotted the fold change of gene expression after ASCC3 knockdown for mRNAs grouped based on the degree of their m⁶A-dependent expression, determined based on fold-change expression after METTL3 inhibition by STM2457. Group of genes that are the most susceptible to m⁶A-mRNA degradation are also the most suppressed after ASCC3 knockdown, suggesting that allowing the collided ribosomes to persist may facilitate m⁶A-mediated mRNA degradation. Two-sided Wilcoxon signed-rank test; ***p < 2e-16. Boxplots show the median, upper/lower quartiles, and whiskers at 1.5× interquartile ranges.

See also Figure S4.

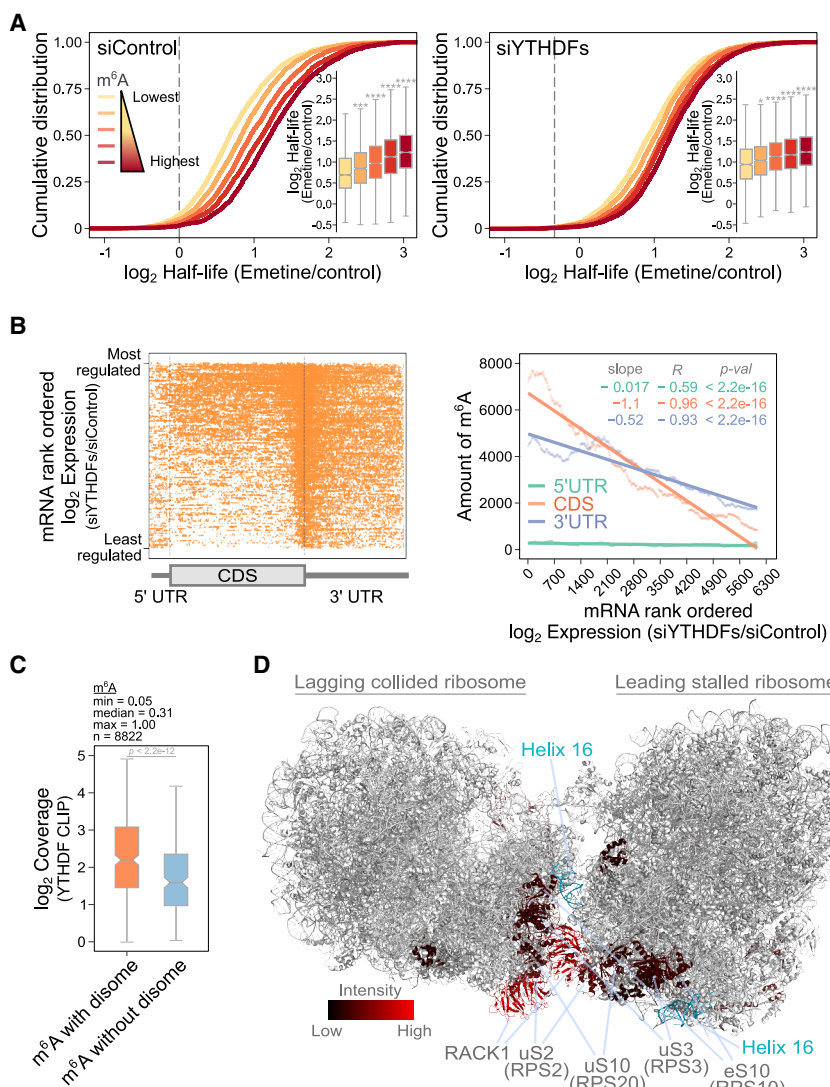


Figure 4. m^6 A-induced ribosome collision may promote YTHDF protein binding for m^6 A-mRNA degradation

(A) mRNA half-life was measured in the absence and presence of emetine in control or *YTHDF* triple knockdown HeLa cells. In control knockdown cells, translation inhibition stabilized mRNA in proportion to the methylation level. However, emetine-induced mRNA stabilization was significantly reduced in *YTHDF* triple knockdown cells. Two-sided Wilcoxon signed-rank test; * $p < 2e-04$, ** $p < 2e-08$, *** $p < 2e-12$, **** $p < 2e-16$. Boxplots show the median, upper/lower quartiles, and whiskers at $1.5 \times$ interquartile ranges.

(B) m^6 A that are encountered by the ribosome more strongly correlate with YTHDF-mediated m^6 A-mRNA degradation. (Left) Similar to Figure 2H, but genes were ranked on the y axis based on their fold-increase in expression in *YTHDF* triple knockdown HeLa cells relative to control knockdown. The location of m^6 A is plotted in each transcript. In mRNAs most regulated by YTHDF proteins, the amount of m^6 A in CDS dropped significantly, while still abundant in 3' UTR. (Right) Quantification of m^6 A levels in the 5' UTR, CDS, and 3' UTR (left).

(C) Ribosome collisions promote YTHDF binding to m^6 A. YTHDF iCLIP signal was quantified over disome-associated m^6 A sites ($n = 8,822$) compared with a control group of CDS m^6 A ($n = 8,822$) on the same set of transcripts ($n = 2,307$) that do not have associated disomes (see STAR Methods). Two-sided Wilcoxon signed-rank test. Boxplots show the median, upper/lower quartiles, and whiskers at $1.5 \times$ interquartile ranges.

(D) Ribosomal subunits identified in a YTHDF protein interactome study⁵⁸ shown in a collided disome structure. The proximity levels of YTHDF² for each ribosomal subunit⁵⁸ were mapped on a cryogenic electron microscopy structure of a collided disome.⁵⁰ Many ribosomal subunits with high levels of YTHDF protein interaction were clustered at the collision interface. Helix 16 of 18S, a YTHDF interaction site identified by iCLIP in Figure S5H is colored in cyan.

See also Figure S5.

whether translation is part of the YTHDF-mediated m^6 A-mRNA degradation pathway. Notably, the stabilizing effect of emetine on m^6 A-mRNAs was markedly reduced in *YTHDF1,2,3* triple knockdown HeLa cells (Figures 4A, S5A, and S5B). Additionally, we found that mRNA stabilization effects of emetine generally correlated with mRNA stabilization effects seen after YTHDF depletion (Figure S5C). These results suggest that mRNA translation and YTHDF proteins function in the same pathway to mediate m^6 A-mRNA degradation.

To further test whether the ability of the ribosome to encounter m^6 A is important for YTHDF-mediated mRNA degradation, we prepared a plot similar to Figure 2H, but ordering mRNAs from the most to least stabilized after YTHDF depletion,¹⁰ and marked the location of m^6 A sites along the length of each transcript. Similar to Figure 2H, we found that CDS m^6 A levels are more strongly correlated with YTHDF-mediated m^6 A-mRNA degradation compared with 3' UTR m^6 A levels (Figure 4B).

We also examined the effect of YTHDF depletion on transcripts that have m^6 A only in the CDS or 3' UTR, similar to Figure S3H. Again, the YTHDF-mediated mRNA degradation effect is more strongly correlated with CDS m^6 A levels compared with 3' UTR m^6 A levels (Figures S5D and S5E).

Since the ribosome is stalled with m^6 A in the A-site of the ribosome, it is likely that the ribosome is the initial sensor of m^6 A. The stalled ribosome, and potentially subsequent collisions, may facilitate YTHDF binding to m^6 A to induce mRNA degradation.

We therefore measured YTHDF binding at m^6 A sites associated with ribosome collisions. We quantified the signal of YTHDF iCLIP, a method for nucleotide-resolution mapping of YTHDF protein-RNA interaction sites, over m^6 A sites that have collided disomes, compared with a control group of CDS m^6 A sites that do not have associated disomes. We found significantly higher YTHDF iCLIP coverage at disome-associated m^6 A sites compared with m^6 A sites without disomes (Figure 4C).

Thus, m⁶A-induced ribosome collisions potentially promote subsequent YTHDF binding to m⁶A.

Next, we wanted to understand how YTHDF proteins may be involved in translation-dependent m⁶A-mRNA degradation. A recent proteomic study of YTHDF interactors suggests that YTHDF proteins interact with the ribosomes through RACK1,⁵⁸ a constitutive component of the 40S subunit.⁵⁹ We asked whether this interaction of YTHDF proteins and RACK1 is related to translation. To test this, we prepared RNase A-treated mESC lysates and measured RACK1 in YTHDF2 immunoprecipitates. As previously reported,⁵⁸ RACK1 was readily detected in YTHDF2 immunoprecipitates (Figure S5G). However, this interaction was substantially reduced when cells are treated with puromycin, a translation inhibitor that disassembles 80S ribosome into 40S and 60S. Thus, the interaction between YTHDF2 and the ribosome may depend on active translation or the 80S structure. Moreover, the YTHDF2-RACK1 interaction depends on m⁶A since this interaction is markedly reduced in *Mettl14* knockout mESC (Figure S5G). The m⁶A dependence of YTHDF2-RACK interactions may reflect initial stalling or collisions at m⁶A sites, which may enhance recruitment of YTHDF2.

Notably, a previous ribosome interactome study also identified YTHDF proteins among proteins that associate with ribosomes, and this interaction was reduced after puromycin treatment.⁶⁰ Additionally, two independent studies of YTHDF protein interactomes found two major interaction networks: RNA degradation proteins including CCR4-NOT deadenylase complex and a group of ribosome-associated proteins.^{58,61} These findings suggest a functional coupling of ribosomes, YTHDF proteins, and subsequent mRNA degradation.

Several studies have shown that the interface of the collided ribosomes acts as a hub to recruit proteins that lead to subsequent effects on cell signaling.^{50,51,62} To visualize a potential interaction site between YTHDF proteins and the collided ribosomes, we used a BiolD study⁵⁸ to identify YTHDF-proximal ribosomal proteins. We color-coded ribosomal proteins on a structure of collided ribosomes⁵⁰ based on their YTHDF2-proximity score.⁵⁸ We found that the ribosomal proteins with the highest YTHDF2 proximity are clustered at the previously defined collision interface,⁵⁰ which comprises RACK1, eS10 (RPS10), uS10 (RPS20), and uS3 (RPS3) (Figures 4D and S5F). Notably, these proteins were found with high proximity to all 3 YTHDF paralogs.⁵⁸

To identify additional potential interactions between YTHDF proteins and the ribosome, we examined YTHDF1,2,3 iCLIP datasets.⁶³ Each YTHDF, but not the nuclear-localized m⁶A reader YTHDC1,⁶³ shows a single common interaction with helix 16 of the 18S rRNA (Figure S5H), located in the area of the ribosome which becomes part of the collision interface (Figure 4D).⁵⁰ Notably, helix 16 lacks any m⁶A site.⁶⁴ Thus, both the YTHDF protein interactomes and RNA interactomes suggest that YTHDF proteins interact with the area of the ribosome that makes up the collision interface.

Stress-induced translation suppression stabilizes m⁶A-mRNAs

We next asked whether cell stress, which leads to only partial reductions in translation,^{65–67} is also able to reduce m⁶A-mRNA degradation and thus lead to increased m⁶A-mRNA levels.

Amino acid depletion (3h) led to translation reduction by ~66% and ~77% in wild-type and *Mettl3* knockout MEFs, respectively (Figure 5A). This condition stabilized mRNAs in proportion to m⁶A levels in each transcript without affecting YTHDF protein levels (Figures 5B, 5C, and S6A). These effects were due to m⁶A since mRNA stabilization was markedly reduced in *Mettl3* knockout MEFs (Figure 5C).

We examined previously published datasets examining gene expression changes in other cell types and other forms of nutrient deprivation.^{69–71} In each case, we also found an increase in the abundance of m⁶A-mRNAs in proportion to m⁶A levels in each transcript (Figure S6B).

Additionally, tunicamycin-induced endoplasmic reticulum stress,⁷² which leads to translational repression⁷³ (Figure S6C), similarly stabilized m⁶A-mRNAs in proportion to m⁶A levels in each transcript^{74,75} (Figure S6D). However, stabilization effects of tunicamycin was less than amino acid depletion (see Figure 5C), likely because amino acid depletion causes larger drops in translation (see Figure S5C).^{76,77}

Overall, these data suggest that the drop in translation elicited by cell stress leads to repressed m⁶A-mediated mRNA degradation and a subsequent increase in m⁶A-mRNA levels.

Suppression of m⁶A-mRNA degradation by cell stress is sufficient to promote autophagy

We next wanted to understand whether m⁶A-mRNA stabilization induced by cellular stress contributes to the adaptive response to stress. Notably, autophagy-related genes are a major Gene Ontology category among the genes that are highly methylated and stabilized in *Mettl3* knockout MEFs (Figure S6E; Table S4). Thus, stabilization of m⁶A-mRNAs induced by cell stress might contribute to the activation of autophagy.

Since amino acid depletion represses m⁶A-mRNA degradation, we examined amino-acid-replete cells that were selectively deficient in m⁶A-mRNA degradation due to *Mettl3* depletion. We measured autophagy by immunostaining for ATG12 and ULK1.^{78,79} As expected, amino acid depletion of wild-type MEFs induced ATG12- and ULK1-labeled puncta (Figures 5D, 5E, S6F, and S6G). However, ATG12 and ULK1-labeled puncta were also readily detected in *Mettl3* knockout MEFs despite being cultured in amino-acid-replete media (Figures 5D, 5E, S6F, and S6G). Thus, impairing m⁶A-mediated mRNA degradation alone is sufficient to induce features of autophagy. Notably, autophagy in *Mettl3* knockout MEFs is not substantially increased further by amino acid depletion (Figures 5E and S6G). These results are consistent with other studies showing increased autophagy in m⁶A-deficient cells.^{4,18,20}

Together, these results suggest that suppression of m⁶A-mediated mRNA is part of the adaptive response to cell stress.

DISCUSSION

Our study shows that m⁶A markedly alters ribosome dynamics and these alterations mediate the destabilizing effect of m⁶A on mRNA. We find that m⁶A promotes ribosome stalling, which is so pronounced that it can lead to ribosome collisions. m⁶A-induced ribosome stalls are influenced by the codon sequence context and the ability of m⁶A to induce stalling correlates to

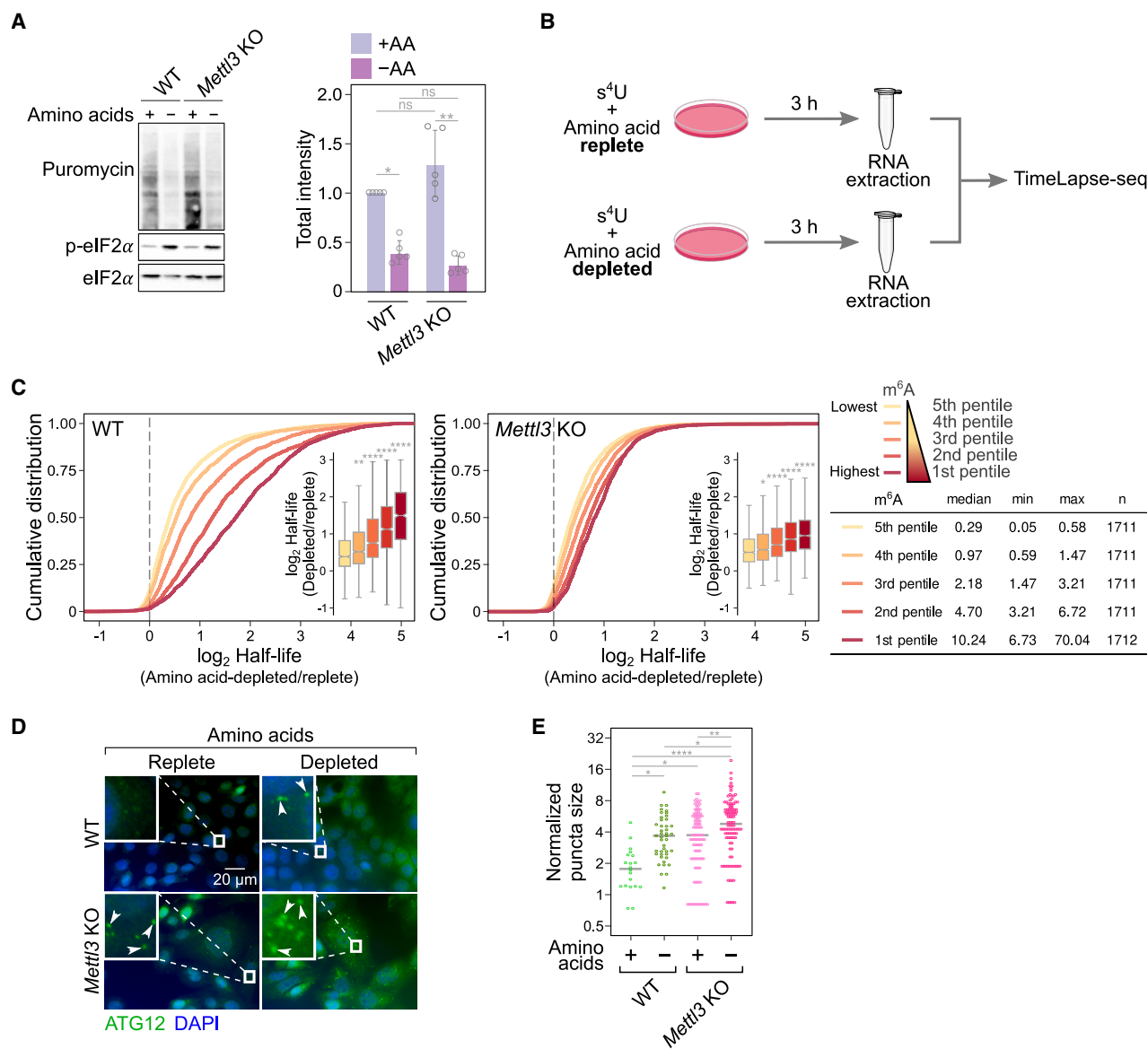


Figure 5. Stress-induced translation suppression stabilizes m⁶A-mRNAs

(A) Amino acid depletion reduces overall translation. (Left) Translation levels were determined by puromycin incorporation after amino acid deletion in wild-type or *Mettl3* knockout MEFs and detected by anti-puromycin immunoblotting. (Right) Quantification of puromycin incorporation. $n = 5$ biological replicates. Two-way ANOVA with Tukey's multiple comparison test; * $p < 0.001$, ** $p < 0.0001$.

(B) Schematic of the TimeLapse-seq experiment.

(C) Amino acid depletion stabilizes m⁶A-mRNAs. Transcripts were grouped into pentiles based on m⁶A levels. The fold change in mRNA half-life after amino acid depletion relative to the amino acid-replete state was measured. mRNA was stabilized in proportion to methylation levels in wild type, but this effect was reduced in *Mettl3* knockout MEFs. Two-sided Wilcoxon signed-rank test; * $p < 2e-04$, ** $p < 2e-08$, *** $p < 2e-12$, **** $p < 2e-16$. Boxplots show the median, upper/lower quartiles, and whiskers at 1.5 \times interquartile ranges.

(D) m⁶A-depleted cells exhibit elevated autophagy levels prior to amino acid depletion. Autophagy was induced in wild-type MEFs after amino acid depletion,⁶⁸ resulting in ATG12-labeled puncta. In *Mettl3* knockout MEFs, ATG12-positive puncta were readily detected in amino-acid-replete conditions, and this only slightly increased after amino acid depletion.

(E) Quantification of ATG12-labeled puncta size in (D). Size of each autophagy puncta was measured and normalized to the cell surface area. One-way ANOVA with Tukey multiple comparison test; * $p < 0.033$, ** $p < 0.0021$, *** $p < 0.00020$, **** $p < 0.00010$.

See also Figure S6.

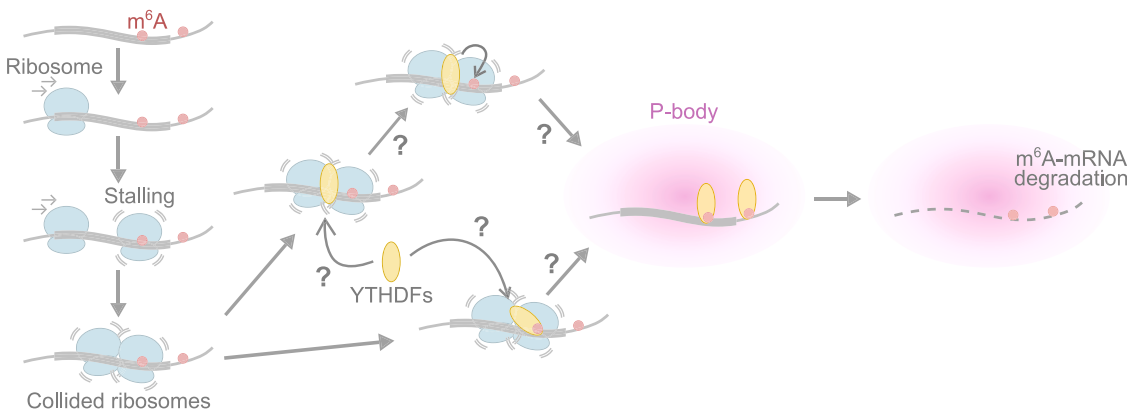


Figure 6. Schematic of m⁶A-induced ribosome collisions and mRNA degradation

m⁶A stalls actively translating ribosomes in the A-site. If the ribosome remains stalled, another ribosome can collide with the stalled ribosome. The collided ribosomes may recruit YTHDF proteins through the collided ribosome interface for eventual binding of YTHDF to m⁶A. The unique footprint of collided ribosomes at m⁶A sites may reflect the influence of YTHDF bound to the collided ribosome or potentially to m⁶A in the A-site. Alternatively, YTHDFs may interact directly with m⁶A in the A-site of the leading ribosome with additional interactions at the collided ribosomes for stable binding. YTHDF at the collided ribosomes may cooperatively stabilize YTHDF binding at other m⁶A, including in the 3' UTR, leading to localization to P-bodies where m⁶A-mRNA degradation is thought to occur.

its ability to induce mRNA degradation. Stalling and the subsequent collisions at m⁶A sites may facilitate YTHDF binding and recruitment of mRNA degradation machinery (Figure 6). This pathway appears to be particularly important during cellular stress, when translation is repressed, and thus reduced stalling and collisions, leads to stabilization of m⁶A-mRNAs. The resulting increase in m⁶A-mRNAs contributes to the adaptive response to stress. Overall, our study reveals that the ribosome is the initial m⁶A sensor, and stalling of the ribosome at m⁶A leads to collisions and potential subsequent YTHDF recruitment, which accounts for the well documented destabilization effect of m⁶A on mRNA.

Emerging studies show that ribosome collisions can have important roles in cellular signaling.^{51,80,81} Ribosome collisions can occur at stop codons,^{44,52} where they may have no functional significance. However, ribosome collisions induced by UV damage form a collision interface that recruits proteins leading to p38 activation.^{51,81} We found that disomes are present in unperturbed cells at m⁶A sites. Thus, m⁶A is an endogenous inducer of ribosome collisions. These collisions may be a critical step in subsequent m⁶A-mRNA degradation since depletion of ASCC3, a protein that is required for disassembly of collided disomes,^{55,82,83} potentiates the degradation effects of m⁶A. The persistence of collided disomes in ASCC3-depleted cells may allow for more efficient YTHDF recruitment and m⁶A-mRNA degradation.

Ribosome collisions at m⁶A appear to adopt a unique conformation compared with previously described disomes.^{44,54} The footprint of m⁶A-induced disomes suggest that the leading ribosome has an altered conformation that allows greater accessibility of the footprinting nuclease to the A-site. As a result, the 3' end of the footprint is only 4–8 nt from the m⁶A-containing A-site. This increased accessibility in the vicinity of A-site is reminiscent of disomes induced by non-optimal codons in yeast, which similarly exhibit a shortened footprint.⁵⁴ However, in these disomes, greater nuclease accessibility was seen in the lagging

ribosome instead of the leading ribosome.⁵⁴ This altered conformation of the lagging ribosome in yeast is thought to allow the Cue2 nuclease to enter the A-site for mRNA cleavage.⁵⁴ Likewise, in the case of m⁶A-induced disomes, the increased accessibility near the m⁶A-containing A-site of the leading ribosome may be functionally important for allowing access of YTHDF proteins to m⁶A. Indeed, we find higher YTHDF iCLIP signals at m⁶A sites associated with disomes compared with m⁶A sites on the same mRNAs lacking mapped disomes, even when controlled for m⁶A stoichiometry.

YTHDF proteins have relatively poor affinity for m⁶A ($K_d \sim 0.7\text{--}2.5 \mu\text{M}$).^{84–86} Direct high-affinity tethering of YTHDF proteins to mRNA reporters promotes the degradation of the reporter mRNA.^{29,87} The disome may similarly recruit YTHDF proteins or stabilize YTHDF interactions with RNA. This may occur via interactions of YTHDF proteins with the collided ribosome interface, which could facilitate eventual binding of YTHDF to m⁶A on the mRNA. Alternatively, YTHDFs may interact directly with m⁶A in the A-site of the stalled ribosome. Disomes may have enough conformational flexibility to allow YTHDF proteins to sample the A-site of the stalled ribosome. If m⁶A is present, YTHDF proteins may bind, which could account for the altered conformation of m⁶A-induced disomes. Structural studies of collided ribosomes that are stalled at m⁶A sites and which have recruited YTHDF proteins will be useful to reveal how YTHDF proteins interact with ribosomes and m⁶A sites.

Although we find that the process of m⁶A-mRNA degradation generally begins with the ribosome encountering m⁶A in the CDS, our data indicate that 3' UTR m⁶A can also contribute to m⁶A-mRNA degradation. Stable binding of YTHDF proteins to m⁶A at collided ribosomes may cooperatively stabilize YTHDF binding at other m⁶A sites, including m⁶A sites in the 3'UTR, for more efficient m⁶A-mRNA degradation. Thus, all m⁶A sites are likely to matter, but an m⁶A site in the CDS initiates the process of degradation due to ribosome stalling and collision.

Translation has long been known to promote degradation of mRNAs^{42,75,88,89} due to non-sense-mediated decay⁹⁰ and codon optimality, which involves stalling at specific codons due to low aminoacyl-tRNA availability.^{42,43} However, our study reveals that the substantial fraction of translation-dependent mRNA degradation in unperturbed cells is caused by m⁶A.

Although m⁶A clearly maintains certain stress-related mRNAs at low levels in normal growth conditions,⁴⁻⁷ the pathways that allow these m⁶A-mRNAs to accumulate when needed for stress responses are poorly understood. Our data suggest that their levels rise due to translational repression, which suppresses the m⁶A-mRNA degradation pathway. Notably, translational repression is a major feature of stress response. Thus, modulation of translation rates may be a key mechanism to control m⁶A-mRNA expression levels and cellular pathways linked to m⁶A.

Limitations of this study

A major challenge is distinguishing whether the stalled ribosome or the subsequent collided ribosomes leads to m⁶A-mRNA degradation since stalling and collisions are linked. Additionally, the timing of YTHDF recruitment to the m⁶A site is difficult to determine. One model is that collided ribosomes recruit YTHDF proteins through the collision interface; alternatively, the collided ribosomes may stabilize YTHDF binding directly to m⁶A in the A-site of the leading ribosome. The unique footprint of collided ribosomes at m⁶A sites may be a key clue. However, it is unclear whether this footprint occurs before YTHDF binding or is a consequence of YTHDF binding. Although YTHDF proteins bind ribosome proteins and rRNA at the collision interface, it is difficult to determine whether these interactions occur during physiologic m⁶A-induced disome formation. Cryogenic electron microscopy using ribosomes collided at m⁶A sites will provide deeper insights into the precise interactions of YTHDF proteins with the m⁶A and the collided ribosomes.

RESOURCE AVAILABILITY

Lead contact

Correspondence and requests for materials should be addressed to Samie R. Jaffrey (srj2003@med.cornell.edu).

Materials availability

Reagents generated in this study are available from the lead contact.

Data and code availability

Sequencing datasets generated in this study are deposited to NCBI Gene Expression Omnibus GEO: GSE249257. Accession numbers for previously published sequencing datasets are provided in the [key resources table](#). The reference genome hg38 and mm10 was downloaded from <https://useast.ensembl.org/index.html>. Ribosome structure was retrieved from the Protein Data Bank (accession numbers PDB: 6HCM, 6HCQ). Original codes are available at GitHub (<https://github.com/shino-mrkm/m6a.translation.git>). Additional information for the data in this study is available upon request to the corresponding author.

ACKNOWLEDGMENTS

We thank J.G. Dumelie, V. Despic, M. Chen, M. Oleynikov, and the rest of the Jaffrey laboratory for helpful comments and discussions; B. Linder for contributions to the early stages of this study; J.G. Dumelie and A. Mirza for unpublished contributions; and the WCM Genomics Resources Core Facility. Sup-

ported by NIH grants S10 OD030335, RM1HG011563, P50HD104454, and R35 NS111631 (to S.R.J.), Moderna Research Fellowship and Department of Defense fellowship BC180715 (to S.M.), and NIH grant K22CA258954 (to S.Z.).

AUTHOR CONTRIBUTIONS

S.M. and S.R.J. conceived the project and designed the experiments unless otherwise stated. S.M. performed all experiments, data analysis, and prepared all the figures. A.O.O.-G., J.F.L., and S.Z. assisted in bioinformatic analysis, and B.H. prepared reagents. S.M. and S.R.J. wrote the manuscript. The manuscript was read and approved by all authors.

DECLARATION OF INTERESTS

S.R.J. is the co-founder, advisor, and/or has equity in Chimerna Therapeutics, 858 Therapeutics, and Lucerna Technologies.

STAR METHODS

Detailed methods are provided in the online version of this paper and include the following:

- KEY RESOURCES TABLE
- EXPERIMENTAL MODEL AND STUDY PARTICIPANT DETAILS
 - Cell culture
- METHOD DETAILS
 - Antibodies
 - Reporter construct cloning
 - Transfection of reporter genes
 - Western blotting
 - Coimmunoprecipitation of YTHDF2
 - RT-qPCR
 - Reanalysis of previously published RNA-seq dataset
 - siRNA-mediated YTHDF1/2/3 knockdown
 - TimeLapse-seq library preparation and sequencing
 - TimeLapse-seq library data analysis
 - m⁶A quantification
 - Library preparation of OTTR ribosome profiling
 - Analysis of OTTR monosome profiling
 - Analysis of OTTR disome profiling
 - Analysis of YTHDF iCLIP datasets
 - Analysis of Toxicogenomic Project database
 - DepMap co-dependency screen
 - Immunofluorescence
 - In vitro ribosome collision assay
 - Disome quantification by sucrose gradient fractionation
 - Visualization of ribosomal subunits identified in YTHDF interactome study on a collided disome
 - Gene Ontology analysis
- QUANTIFICATION AND STATISTICAL ANALYSIS

SUPPLEMENTAL INFORMATION

Supplemental information can be found online at <https://doi.org/10.1016/j.cell.2025.04.020>.

Received: August 1, 2024

Revised: December 14, 2024

Accepted: April 14, 2025

Published: May 5, 2025

REFERENCES

1. Poh, H.X., Mirza, A.H., Pickering, B.F., and Jaffrey, S.R. (2022). Alternative splicing of METTL3 explains apparently METTL3-independent m⁶A modifications in mRNA. *PLoS Biol.* 20, e3001683. <https://doi.org/10.1371/journal.pbio.3001683>.

2. Geula, S., Moshitch-Moshkovitz, S., Dominissini, D., Mansour, A.A., Kol, N., Salmon-Divon, M., Hershkovitz, V., Peer, E., Mor, N., Manor, Y.S., et al. (2015). m⁶A mRNA methylation facilitates resolution of naïve pluripotency toward differentiation. *Science* 347, 1002–1006. <https://doi.org/10.1126/science.1261417>.
3. Ries, R.J., Zaccara, S., Klein, P., Olarerin-George, A., Namkoong, S., Pickering, B.F., Patil, D.P., Kwak, H., Lee, J.H., and Jaffrey, S.R. (2019). m⁶A enhances the phase separation potential of mRNA. *Nature* 571, 424–428. <https://doi.org/10.1038/s41586-019-1374-1>.
4. Li, G., Deng, L., Huang, N., Cui, Z., Wu, Q., Ma, J., Pan, Q., and Sun, F. (2021). m⁶A mRNA Methylation Regulates LKB1 to Promote Autophagy of Hepatoblastoma Cells through Upregulated Phosphorylation of AMPK. *Genes* 12, 1747. <https://doi.org/10.3390/genes12111747>.
5. Fry, N.J., Law, B.A., Ilkayeva, O.R., Holley, C.L., and Mansfield, K.D. (2017). N⁶-methyladenosine is required for the hypoxic stabilization of specific mRNAs. *RNA* 23, 1444–1455. <https://doi.org/10.1261/rna.061044.117>.
6. Rubio, R.M., Depledge, D.P., Bianco, C., Thompson, L., and Mohr, I. (2018). RNA m6 A modification enzymes shape innate responses to DNA by regulating interferon β . *Genes Dev.* 32, 1472–1484. <https://doi.org/10.1101/gad.319475.118>.
7. Yu, R., Li, Q., Feng, Z., Cai, L., and Xu, Q. (2019). m⁶A Reader YTHDF2 Regulates LPS-Induced Inflammatory Response. *Int. J. Mol. Sci.* 20, 1323. <https://doi.org/10.3390/ijms20061323>.
8. Bokar, J.A., Shambaugh, M.E., Polayes, D., Matera, A.G., and Rottman, F.M. (1997). Purification and cDNA cloning of the AdoMet-binding subunit of the human mRNA (N⁶-adenosine)-methyltransferase. *RNA* 3, 1233–1247.
9. Sommer, S., Lavi, U., and Darnell, J.E. (1978). The absolute frequency of labeled N-6-methyladenosine in HeLa cell messenger RNA decreases with label time. *J. Mol. Biol.* 124, 487–499. [https://doi.org/10.1016/0022-2836\(78\)90183-3](https://doi.org/10.1016/0022-2836(78)90183-3).
10. Zaccara, S., and Jaffrey, S.R. (2020). A Unified Model for the Function of YTHDF Proteins in Regulating m⁶A-Modified mRNA. *Cell* 181, 1582–1595.e18. <https://doi.org/10.1016/j.cell.2020.05.012>.
11. Murakami, S., and Jaffrey, S.R. (2022). Hidden codes in mRNA: Control of gene expression by m⁶A. *Mol. Cell* 82, 2236–2251. <https://doi.org/10.1016/j.molcel.2022.05.029>.
12. Salisbury, D.A., Casero, D., Zhang, Z., Wang, D., Kim, J., Wu, X., Vergnes, L., Mirza, A.H., Leon-Mimila, P., Williams, K.J., et al. (2021). Transcriptional regulation of N⁶-methyladenosine orchestrates sex-dimorphic metabolic traits. *Nat. Metab.* 3, 940–953. <https://doi.org/10.1038/s42255-021-00427-2>.
13. Wang, S., Chen, S., Sun, J., Han, P., Xu, B., Li, X., Zhong, Y., Xu, Z., Zhang, P., Mi, P., et al. (2023). m⁶A modification-tuned sphingolipid metabolism regulates postnatal liver development in male mice. *Nat. Metab.* 5, 842–860. <https://doi.org/10.1038/s42255-023-00808-9>.
14. Raj, N., Wang, M., Seoane, J.A., Zhao, R.L., Kaiser, A.M., Moonie, N.A., Demeter, J., Boutelle, A.M., Kerr, C.H., Mulligan, A.S., et al. (2022). The Mettl3 epitranscriptomic writer amplifies p53 stress responses. *Mol. Cell* 82, 2370–2384.e10. <https://doi.org/10.1016/j.molcel.2022.04.010>.
15. Wang, X., Wu, R., Liu, Y., Zhao, Y., Bi, Z., Yao, Y., Liu, Q., Shi, H., Wang, F., and Wang, Y. (2020). m⁶A mRNA methylation controls autophagy and adipogenesis by targeting Atg5 and Atg7. *Autophagy* 16, 1221–1235. <https://doi.org/10.1080/15548627.2019.1659617>.
16. Shu, X.E., Swanda, R.V., and Qian, S.-B. (2020). Nutrient Control of mRNA Translation. *Annu. Rev. Nutr.* 40, 51–75. <https://doi.org/10.1146/annurev-nutr-120919-041411>.
17. Zhong, X., Yu, J., Frazier, K., Weng, X., Li, Y., Cham, C.M., Dolan, K., Zhu, X., Hubert, N., Tao, Y., et al. (2018). Circadian Clock Regulation of Hepatic Lipid Metabolism by Modulation of m⁶A mRNA Methylation. *Cell Rep.* 25, 1816–1828.e4. <https://doi.org/10.1016/j.celrep.2018.10.068>.
18. Song, H., Feng, X., Zhang, H., Luo, Y., Huang, J., Lin, M., Jin, J., Ding, X., Wu, S., Huang, H., et al. (2019). METTL3 and ALKBH5 oppositely regulate m⁶A modification of TFEB mRNA, which dictates the fate of hypoxia/reoxygenation-treated cardiomyocytes. *Autophagy* 15, 1419–1437. <https://doi.org/10.1080/15548627.2019.1586246>.
19. Li, G., Song, Y., Liao, Z., Wang, K., Luo, R., Lu, S., Zhao, K., Feng, X., Liang, H., Ma, L., et al. (2020). Bone-derived mesenchymal stem cells alleviate compression-induced apoptosis of nucleus pulposus cells by N⁶-methyladenosine of autophagy. *Cell Death Dis.* 11, 103. <https://doi.org/10.1038/s41419-020-2284-8>.
20. Cao, Z., Zhang, L., Hong, R., Li, Y., Wang, Y., Qi, X., Ning, W., Gao, D., Xu, T., Ma, Y., et al. (2021). METTL3-mediated m⁶A methylation negatively modulates autophagy to support porcine blastocyst development. *Biol. Reprod.* 104, 1008–1021. <https://doi.org/10.1093/biolre/ioab022>.
21. Chen, X., Gong, W., Shao, X., Shi, T., Zhang, L., Dong, J., Shi, Y., Shen, S., Qin, J., Jiang, Q., et al. (2022). METTL3-mediated m⁶A modification of ATG7 regulates autophagy-GATA4 axis to promote cellular senescence and osteoarthritis progression. *Ann. Rheum. Dis.* 81, 87–99. <https://doi.org/10.1136/annrheumdis-2021-221091>.
22. Barak, Y., Juven, T., Haffner, R., and Oren, M. (1993). mdm2 expression is induced by wild type p53 activity. *EMBO J.* 12, 461–468. <https://doi.org/10.1002/j.1460-2075.1993.tb05678.x>.
23. Khambu, B., Uesugi, M., and Kawazoe, Y. (2011). Translational repression stabilizes messenger RNA of autophagy-related genes. *Genes Cells* 16, 857–867. <https://doi.org/10.1111/j.1365-2443.2011.01532.x>.
24. Xu, L., Zhang, X., Tian, Y., Fan, Z., Li, W., Liu, M., Hu, J., Duan, Z., Jin, R., and Ren, F. (2020). The critical role of PPAR α in the binary switch between life and death induced by endoplasmic reticulum stress. *Cell Death Dis.* 11, 691. <https://doi.org/10.1038/s41419-020-02811-4>.
25. Peter, A., Weigert, C., Staiger, H., Machicao, F., Schick, F., Machann, J., Stefan, N., Thamer, C., Häring, H.-U., and Schleicher, E. (2009). Individual Stearyl-CoA Desaturase 1 Expression Modulates Endoplasmic Reticulum Stress and Inflammation in Human Myotubes and Is Associated With Skeletal Muscle Lipid Storage and Insulin Sensitivity In Vivo. *Diabetes* 58, 1757–1765. <https://doi.org/10.2337/db09-0188>.
26. Pei, G., Zyla, J., He, L., Moura-Alves, P., Steinle, H., Saikali, P., Lozza, L., Nieuwenhuizen, N., Weiner, J., Mollenkopf, H.J., et al. (2021). Cellular stress promotes NOD1/2-dependent inflammation via the endogenous metabolite sphingosine-1-phosphate. *EMBO J.* 40, e106272. <https://doi.org/10.15252/embj.2020106272>.
27. Velasco-Miguel, S., Richardson, J.A., Gerlach, V.L., Lai, W.C., Gao, T., Russell, L.D., Hladik, C.L., White, C.L., and Friedberg, E.C. (2003). Constitutive and regulated expression of the mouse *Dinb* (*Polk*) gene encoding DNA polymerase kappa. *DNA Repair* 2, 91–106. [https://doi.org/10.1016/S1568-7868\(02\)00189-1](https://doi.org/10.1016/S1568-7868(02)00189-1).
28. Contreras, P.S., Tapia, P.J., Jeong, E., Ghosh, S., Altan-Bonnet, N., and Puertollano, R. (2023). Beta-coronaviruses exploit cellular stress responses by modulating TFEB and TFE3 activity. *iScience* 26, 106169. <https://doi.org/10.1016/j.isci.2023.106169>.
29. Du, H., Zhao, Y., He, J., Zhang, Y., Xi, H., Liu, M., Ma, J., and Wu, L. (2016). YTHDF2 destabilizes m⁶A-containing RNA through direct recruitment of the CCR4-NOT deadenylase complex. *Nat. Commun.* 7, 12626. <https://doi.org/10.1038/ncomms12626>.
30. Park, O.H., Ha, H., Lee, Y., Boo, S.H., Kwon, D.H., Song, H.K., and Kim, Y.K. (2019). Endoribonucleolytic Cleavage of m⁶A-Containing RNAs by RNase P/MRP Complex. *Mol. Cell* 74, 494–507.e8. <https://doi.org/10.1016/j.molcel.2019.02.034>.
31. Choi, J., leong, K.-W., Demirci, H., Chen, J., Petrov, A., Prabhakar, A., O'Leary, S.E., Dominissini, D., Rechavi, G., Soltis, S.M., et al. (2016). N⁶-methyladenosine in mRNA disrupts tRNA selection and translation-elongation dynamics. *Nat. Struct. Mol. Biol.* 23, 110–115. <https://doi.org/10.1038/nsmb.3148>.
32. Jain, S., Koziej, L., Poulis, P., Kaczmarczyk, I., Gaik, M., Rawski, M., Ranjan, N., Glatt, S., and Rodnina, M.V. (2023). Modulation of translational

- decoding by m⁶A modification of mRNA. *Nat. Commun.* 14, 4784. <https://doi.org/10.1038/s41467-023-40422-7>.
33. Mao, Y., Dong, L., Liu, X.-M., Guo, J., Ma, H., Shen, B., and Qian, S.-B. (2019). m⁶A in mRNA coding regions promotes translation via the RNA helicase-containing YTHDC2. *Nat. Commun.* 10, 5332. <https://doi.org/10.1038/s41467-019-13317-9>.
34. Zhou, Y., Čorović, M., Hoch-Kraft, P., Meiser, N., Mesitov, M., Körtel, N., Back, H., Naarmann-de Vries, I.S., Katti, K., Obřdík, A., et al. (2024). m⁶A sites in the coding region trigger translation-dependent mRNA decay. *Mol. Cell* 84, 4576–4593.e12. <https://doi.org/10.1016/j.molcel.2024.10.033>.
35. Igarashi, Y., Nakatsu, N., Yamashita, T., Ono, A., Ohno, Y., Urushidani, T., and Yamada, H. (2015). Open TG-GATEs: a large-scale toxicogenomics database. *Nucleic Acids Res.* 43, D921–D927. <https://doi.org/10.1093/nar/gku955>.
36. Boulias, K., Toczydłowska-Socha, D., Hawley, B.R., Liberman, N., Takashima, K., Zaccara, S., Guez, T., Vasseur, J.-J., Debart, F., Aravind, L., et al. (2019). Identification of the m⁶Am Methyltransferase PCIF1 Reveals the Location and Functions of m⁶Am in the Transcriptome. *Mol. Cell* 75, 631–643.e8. <https://doi.org/10.1016/j.molcel.2019.06.006>.
37. Liu, C., Sun, H., Yi, Y., Shen, W., Li, K., Xiao, Y., Li, F., Li, Y., Hou, Y., Lu, B., et al. (2023). Absolute quantification of single-base m⁶A methylation in the mammalian transcriptome using GLORI. *Nat. Biotechnol.* 41, 355–366. <https://doi.org/10.1038/s41587-022-01487-9>.
38. Ghandi, M., Huang, F.W., Jané-Valbuena, J., Kryukov, G.V., Lo, C.C., McDonald, E.R., Barretina, J., Gelfand, E.T., Bielski, C.M., Li, H., et al. (2019). Next-generation characterization of the Cancer Cell Line Encyclopedia. *Nature* 569, 503–508. <https://doi.org/10.1038/s41586-019-1186-3>.
39. Meyers, R.M., Bryan, J.G., McFarland, J.M., Weir, B.A., Sizemore, A.E., Xu, H., Dharia, N.V., Montgomery, P.G., Cowley, G.S., Pantel, S., et al. (2017). Computational correction of copy number effect improves specificity of CRISPR-Cas9 essentiality screens in cancer cells. *Nat. Genet.* 49, 1779–1784. <https://doi.org/10.1038/ng.3984>.
40. Dempster, J.M., Rossen, J., Kazachkova, M., Pan, J., Kugener, G., Root, D.E., and Tsherniak, A. (2019). Extracting Biological Insights from the Project Achilles Genome-Scale CRISPR Screens in Cancer Cell Lines. Preprint at bioRxiv. <https://doi.org/10.1101/720243>.
41. Fritz, S.E., Ranganathan, S., Wang, C.D., and Hogg, J.R. (2022). An alternative UPF1 isoform drives conditional remodeling of nonsense-mediated mRNA decay. *EMBO J.* 41, e108898. <https://doi.org/10.15252/embj.2021108898>.
42. Wu, Q., Medina, S.G., Kushawah, G., DeVore, M.L., Castellano, L.A., Hand, J.M., Wright, M., and Bazzini, A.A. (2019). Translation affects mRNA stability in a codon-dependent manner in human cells. *eLife* 8, e45396. <https://doi.org/10.7554/eLife.45396>.
43. Hia, F., Yang, S.F., Shichino, Y., Yoshinaga, M., Murakawa, Y., Vandenberg, A., Fukao, A., Fujiwara, T., Landthaler, M., Natsume, T., et al. (2019). Codon bias confers stability to human mRNAs. *EMBO Rep.* 20, e48220. <https://doi.org/10.15252/embr.201948220>.
44. Ferguson, L., Upton, H.E., Pimentel, S.C., Mok, A., Lareau, L.F., Collins, K., and Ingolia, N.T. (2023). Streamlined and sensitive mono- and di-ribosome profiling in yeast and human cells. *Nat. Methods* 20, 1704–1715. <https://doi.org/10.1038/s41592-023-02028-1>.
45. Meyer, K.D., Saleto, Y., Zumbo, P., Elemento, O., Mason, C.E., and Jaffrey, S.R. (2012). Comprehensive Analysis of mRNA Methylation Reveals Enrichment in 3' UTRs and near Stop Codons. *Cell* 149, 1635–1646. <https://doi.org/10.1016/j.cell.2012.05.003>.
46. Dominissini, D., Moshitch-Moshkovitz, S., Schwartz, S., Salmon-Divon, M., Ungar, L., Osenberg, S., Cesarkas, K., Jacob-Hirsch, J., Amariglio, N., Kupiec, M., et al. (2012). Topology of the human and mouse m⁶A RNA methylomes revealed by m⁶A-seq. *Nature* 485, 201–206. <https://doi.org/10.1038/nature11112>.
47. Rücklé, C., Körtel, N., Basilicata, M.F., Busch, A., Zhou, Y., Hoch-Kraft, P., Tretow, K., Kielisch, F., Bertin, M., Pradhan, M., et al. (2023). RNA stability controlled by m⁶A methylation contributes to X-to-autosome dosage compensation in mammals. *Nat. Struct. Mol. Biol.* 30, 1207–1215. <https://doi.org/10.1038/s41594-023-00997-7>.
48. Yankova, E., Blackaby, W., Albertella, M., Rak, J., De Braekeleer, E., Tsagkogeorga, G., Pilka, E.S., Aspris, D., Leggate, D., Hendrick, A.G., et al. (2021). Small-molecule inhibition of METTL3 as a strategy against myeloid leukaemia. *Nature* 593, 597–601. <https://doi.org/10.1038/s41586-021-03536-w>.
49. Presnyak, V., Alhusaini, N., Chen, Y.-H., Martin, S., Morris, N., Kline, N., Olson, S., Weinberg, D., Baker, K.E., Graveley, B.R., et al. (2015). Codon Optimality Is a Major Determinant of mRNA Stability. *Cell* 160, 1111–1124. <https://doi.org/10.1016/j.cell.2015.02.029>.
50. Juszkiewicz, S., Chandrasekaran, V., Lin, Z., Kraatz, S., Ramakrishnan, V., and Hegde, R.S. (2018). ZNF598 Is a Quality Control Sensor of Collided Ribosomes. *Mol. Cell* 72, 469–481.e7. <https://doi.org/10.1016/j.molcel.2018.08.037>.
51. Wu, C.C.-C., Peterson, A., Zinshteyn, B., Regot, S., and Green, R. (2020). Ribosome Collisions Trigger General Stress Responses to Regulate Cell Fate. *Cell* 182, 404–416.e14. <https://doi.org/10.1016/j.cell.2020.06.006>.
52. Han, P., Shichino, Y., Schneider-Poetsch, T., Mito, M., Hashimoto, S., Udagawa, T., Kohno, K., Yoshida, M., Mishima, Y., Inada, T., et al. (2020). Genome-wide Survey of Ribosome Collision. *Cell Rep.* 31, 107610. <https://doi.org/10.1016/j.celrep.2020.107610>.
53. Wu, C.C.-C., Zinshteyn, B., Wehner, K.A., and Green, R. (2019). High-Resolution Ribosome Profiling Defines Discrete Ribosome Elongation States and Translational Regulation during Cellular Stress. *Mol. Cell* 73, 959–970.e5. <https://doi.org/10.1016/j.molcel.2018.12.009>.
54. D'Orazio, K.N., Wu, C.C.-C., Sinha, N.K., Loll-Krippleber, R., Brown, G.W., and Green, R. (2019). The endonuclease Cue2 cleaves mRNAs at stalled ribosomes during No Go Decay. *eLife* 8, e49117. <https://doi.org/10.7554/eLife.49117>.
55. Juszkiewicz, S., Speldewinde, S.H., Wan, L., Svejstrup, J.Q., and Hegde, R.S. (2020). The ASC-1 Complex Disassembles Collided Ribosomes. *Mol. Cell* 79, 603–614.e8. <https://doi.org/10.1016/j.molcel.2020.06.006>.
56. Kito, Y., Matsumoto, A., Ichihara, K., Shiraishi, C., Tang, R., Hatano, A., Matsumoto, M., Han, P., Iwasaki, S., and Nakayama, K.I. (2023). The ASC-1 complex promotes translation initiation by scanning ribosomes. *EMBO J.* 42, e112869. <https://doi.org/10.15252/embj.2022112869>.
57. Lasman, L., Krupalnik, V., Viukov, S., Mor, N., Aguilera-Castrejon, A., Schneir, D., Bayerl, J., Mizrahi, O., Peles, S., Tawil, S., et al. (2020). Context-dependent functional compensation between Ythdf m⁶A reader proteins. *Genes Dev.* 34, 1373–1391. <https://doi.org/10.1101/gad.340695.120>.
58. Moch, C., Zou, L., Pythoud, N., Fillon, E., Bourgeois, G., Graille, M., Carapito, C., and Chapat, C. (2023). The YTHDF1-3 proteins are bidirectionally influenced by the codon content of their mRNA targets. Preprint at bioRxiv. <https://doi.org/10.1101/2023.11.20.565808>.
59. Johnson, A.G., Lapointe, C.P., Wang, J., Corsepius, N.C., Choi, J., Fuchs, G., and Puglisi, J.D. (2019). RACK1 on and off the ribosome. *RNA* 25, 881–895. <https://doi.org/10.1261/rna.071217.119>.
60. Simsek, D., Tiu, G.C., Flynn, R.A., Byeon, G.W., Leppek, K., Xu, A.F., Chang, H.Y., and Barna, M. (2017). The Mammalian Ribo-interactome Reveals Ribosome Functional Diversity and Heterogeneity. *Cell* 169, 1051–1065.e18. <https://doi.org/10.1016/j.cell.2017.05.022>.
61. Youn, J.-Y., Dunham, W.H., Hong, S.J., Knight, J.D.R., Bashkurov, M., Chen, G.I., Bagci, H., Rathod, B., MacLeod, G., Eng, S.W.M., et al. (2018). High-Density Proximity Mapping Reveals the Subcellular Organization of mRNA-Associated Granules and Bodies. *Mol. Cell* 69, 517–532.e11. <https://doi.org/10.1016/j.molcel.2017.12.020>.
62. Sinha, N.K., Ordureau, A., Best, K., Saba, J.A., Zinshteyn, B., Sundaramoorthy, E., Fulzele, A., Garshott, D.M., Denk, T., Thoms, M., et al.

- (2020). EDF1 coordinates cellular responses to ribosome collisions. *eLife* 9, e58828. <https://doi.org/10.7554/eLife.58828>.
63. Patil, D.P., Chen, C.-K., Pickering, B.F., Chow, A., Jackson, C., Guttman, M., and Jaffrey, S.R. (2016). m⁶A RNA methylation promotes XIST-mediated transcriptional repression. *Nature* 537, 369–373. <https://doi.org/10.1038/nature19342>.
64. Holvec, S., Barchet, C., Lechner, A., Fréchin, L., De Silva, S.N.T., Hazemann, I., Wolff, P., von Loefelholz, O., and Klaholz, B.P. (2024). The structure of the human 80S ribosome at 1.9 Å resolution reveals the molecular role of chemical modifications and ions in RNA. *Nat. Struct. Mol. Biol.* 31, 1251–1264. <https://doi.org/10.1038/s41594-024-01274-x>.
65. Darnell, A.M., Subramanian, A.R., and O'Shea, E.K. (2018). Translational Control through Differential Ribosome Pausing during Amino Acid Limitation in Mammalian Cells. *Mol. Cell* 71, 229–243.e11. <https://doi.org/10.1016/j.molcel.2018.06.041>.
66. Pavlova, N.N., King, B., Josselson, R.H., Violante, S., Macera, V.L., Varadhana, S.A., Cross, J.R., and Thompson, C.B. (2020). Translation in amino-acid-poor environments is limited by tRNAGln charging. *eLife* 9, e62307. <https://doi.org/10.7554/eLife.62307>.
67. Coots, R.A., Liu, X.-M., Mao, Y., Dong, L., Zhou, J., Wan, J., Zhang, X., and Qian, S.-B. (2017). m⁶A Facilitates eIF4F-Independent mRNA Translation. *Mol. Cell* 68, 504–514.e7. <https://doi.org/10.1016/j.molcel.2017.10.002>.
68. Tian, W., Alsaadi, R., Guo, Z., Kalinina, A., Carrier, M., Tremblay, M.-E., Lacoste, B., Lagace, D., and Russell, R.C. (2020). An antibody for analysis of autophagy induction. *Nat. Methods* 17, 232–239. <https://doi.org/10.1038/s41592-019-0661-y>.
69. Kim, D., Kim, J., Yu, Y.S., Kim, Y.R., Baek, S.H., and Won, K.-J. (2022). Systemic approaches using single cell transcriptome reveal that C/EBPγ regulates autophagy under amino acid starved condition. *Nucleic Acids Res.* 50, 7298–7309. <https://doi.org/10.1093/nar/gkac593>.
70. Goldsmith, J., Marsh, T., Asthana, S., Leidal, A.M., Suresh, D., Olshan, A., and Debnath, J. (2020). Ribosome profiling reveals a functional role for autophagy in mRNA translational control. *Commun. Biol.* 3, 388. <https://doi.org/10.1038/s42003-020-1090-2>.
71. Peeters, J.G.C., Picavet, L.W., Coenen, S.G.J.M., Mauthe, M., Vervoort, S.J., Mocholi, E., de Heus, C., Klumperman, J., Vastert, S.J., Reggiori, F., et al. (2019). Transcriptional and epigenetic profiling of nutrient-deprived cells to identify novel regulators of autophagy. *Autophagy* 15, 98–112. <https://doi.org/10.1080/15548627.2018.1509608>.
72. Takatsuki, A., and Tamura, G. (1971). Effect of tunicamycin on the synthesis of macromolecules in cultures of chick embryo fibroblasts infected with Newcastle disease virus. *J. Antibiot. (Tokyo)* 24, 785–794. <https://doi.org/10.7164/antibiotics.24.785>.
73. Harding, H.P., Zhang, Y., Bertolotti, A., Zeng, H., and Ron, D. (2000). PERK Is Essential for Translational Regulation and Cell Survival during the Unfolded Protein Response. *Mol. Cell* 5, 897–904. [https://doi.org/10.1016/S1097-2765\(00\)80330-5](https://doi.org/10.1016/S1097-2765(00)80330-5).
74. Torrence, M.E., MacArthur, M.R., Hosios, A.M., Valvezan, A.J., Asara, J. M., Mitchell, J.R., and Manning, B.D. (2021). The mTORC1-mediated activation of ATF4 promotes protein and glutathione synthesis downstream of growth signals. *eLife* 10, e63326. <https://doi.org/10.7554/eLife.63326>.
75. Wang, D., Zavadil, J., Martin, L., Parisi, F., Friedman, E., Levy, D., Harding, H., Ron, D., and Gardner, L.B. (2011). Inhibition of Nonsense-Mediated RNA Decay by the Tumor Microenvironment Promotes Tumorigenesis. *Mol. Cell. Biol.* 31, 3670–3680. <https://doi.org/10.1128/MCB.05704-11>.
76. Allen, R.E., Raines, P.L., and Regen, D.M. (1969). Regulatory significance of transfer RNA charging levels. I. Measurements of charging levels in livers of chow-fed rats, fasting rats, and rats fed balanced or imbalanced mixtures of amino acids. *Biochim. Biophys. Acta* 190, 323–336. [https://doi.org/10.1016/0005-2787\(69\)90083-5](https://doi.org/10.1016/0005-2787(69)90083-5).
77. Vaughan, M.H., and Hansen, B.S. (1973). Control of initiation of protein synthesis in human cells. Evidence for a role of uncharged transfer ribonucleic acid. *J. Biol. Chem.* 248, 7087–7096. [https://doi.org/10.1016/S0021-9258\(19\)43365-6](https://doi.org/10.1016/S0021-9258(19)43365-6).
78. Hara, T., Takamura, A., Kishi, C., Iemura, S.-I., Natsume, T., Guan, J.-L., and Mizushima, N. (2008). FIP200, a ULK-interacting protein, is required for autophagosome formation in mammalian cells. *J. Cell Biol.* 181, 497–510. <https://doi.org/10.1083/jcb.200712064>.
79. Moreau, K., Ravikumar, B., Renna, M., Puri, C., and Rubinsztein, D.C. (2011). Autophagosome Precursor Maturation Requires Homotypic Fusion. *Cell* 146, 303–317. <https://doi.org/10.1016/j.cell.2011.06.023>.
80. Boon, N.J., Oliveira, R.A., Körner, P.-R., Kochavi, A., Mertens, S., Malka, Y., Voogd, R., van der Horst, S.E.M., Huismans, M.A., Smabers, L.P., et al. (2024). DNA damage induces p53-independent apoptosis through ribosome stalling. *Science* 384, 785–792. <https://doi.org/10.1126/science.adh7950>.
81. Sinha, N.K., McKenney, C., Yeow, Z.Y., Li, J.J., Nam, K.H., Yaron-Barir, T.M., Johnson, J.L., Huntsman, E.M., Cantley, L.C., Ordureau, A., et al. (2024). The ribotoxic stress response drives UV-mediated cell death. *Cell* 187, 3652–3670.e40. <https://doi.org/10.1016/j.cell.2024.05.018>.
82. Matsuo, Y., Tesina, P., Nakajima, S., Mizuno, M., Endo, A., Buschauer, R., Cheng, J., Shounai, O., Ikeuchi, K., Saeki, Y., et al. (2020). RQT complex dissociates ribosomes collided on endogenous RQC substrate SDD1. *Nat. Struct. Mol. Biol.* 27, 323–332. <https://doi.org/10.1038/s41594-020-0393-9>.
83. Best, K., Ikeuchi, K., Kater, L., Best, D., Musial, J., Matsuo, Y., Berninghausen, O., Becker, T., Inada, T., and Beckmann, R. (2023). Structural basis for clearing of ribosome collisions by the RQT complex. *Nat. Commun.* 14, 921. <https://doi.org/10.1038/s41467-023-36230-8>.
84. Xu, C., Liu, K., Ahmed, H., Loppnau, P., Schapira, M., and Min, J. (2015). Structural Basis for the Discriminative Recognition of N⁶-Methyladenosine RNA by the Human YT521-B Homology Domain Family of Proteins. *J. Biol. Chem.* 290, 24902–24913. <https://doi.org/10.1074/jbc.M115.680389>.
85. Zhu, T., Roundtree, I.A., Wang, P., Wang, X., Wang, L., Sun, C., Tian, Y., Li, J., He, C., and Xu, Y. (2014). Crystal structure of the YTH domain of YTHDF2 reveals mechanism for recognition of N⁶-methyladenosine. *Cell Res.* 24, 1493–1496. <https://doi.org/10.1038/cr.2014.152>.
86. Li, F., Zhao, D., Wu, J., and Shi, Y. (2014). Structure of the YTH domain of human YTHDF2 in complex with an m⁶A mononucleotide reveals an aromatic cage for m⁶A recognition. *Cell Res.* 24, 1490–1492. <https://doi.org/10.1038/cr.2014.153>.
87. Wang, X., Lu, Z., Gomez, A., Hon, G.C., Yue, Y., Han, D., Fu, Y., Parisien, M., Dai, Q., Jia, G., et al. (2014). N⁶-methyladenosine-dependent regulation of messenger RNA stability. *Nature* 505, 117–120. <https://doi.org/10.1038/nature12730>.
88. Hu, W., Sweet, T.J., Chamnongpol, S., Baker, K.E., and Coller, J. (2009). Co-translational mRNA decay in *Saccharomyces cerevisiae*. *Nature* 461, 225–229. <https://doi.org/10.1038/nature08265>.
89. Dave, P., Roth, G., Griesbach, E., Mateju, D., Hochstoeger, T., and Chao, J.A. (2023). Single-molecule imaging reveals translation-dependent destabilization of mRNAs. *Mol. Cell* 83, 589–606.e6. <https://doi.org/10.1016/j.molcel.2023.01.013>.
90. Sachs, A.B. (1993). Messenger RNA degradation in eukaryotes. *Cell* 74, 413–421. [https://doi.org/10.1016/0092-8674\(93\)80043-E](https://doi.org/10.1016/0092-8674(93)80043-E).
91. Ke, S., Pandya-Jones, A., Saito, Y., Fak, J.J., Vågbo, C.B., Geula, S., Hanna, J.H., Black, D.L., Darnell, J.E., and Darnell, R.B. (2017). m⁶A mRNA modifications are deposited in nascent pre-mRNA and are not required for splicing but do specify cytoplasmic turnover. *Genes Dev.* 31, 990–1006. <https://doi.org/10.1101/gad.301036.117>.
92. Ries, R.J., Pickering, B.F., Poh, H.X., Namkoong, S., and Jaffrey, S.R. (2023). m⁶A governs length-dependent enrichment of mRNAs in stress

- granules. *Nat. Struct. Mol. Biol.* 30, 1525–1535. <https://doi.org/10.1038/s41594-023-01089-2>.
93. Love, M.I., Huber, W., and Anders, S. (2014). Moderated estimation of fold change and dispersion for RNA-seq data with DESeq2. *Genome Biol.* 15, 550. <https://doi.org/10.1186/s13059-014-0550-8>.
94. R Core Team (2021). *R: A Language and Environment for Statistical Computing* (R Foundation for Statistical Computing).
95. Ewels, P., Magnusson, M., Lundin, S., and Käller, M. (2016). MultiQC: summarize analysis results for multiple tools and samples in a single report. *Bioinformatics* 32, 3047–3048. <https://doi.org/10.1093/bioinformatics/btw354>.
96. Simon, A. (2010). Babraham Bioinformatics - FastQC A Quality Control tool for High Throughput Sequence Data. <http://www.bioinformatics.babraham.ac.uk/projects/fastqc/>.
97. Neumann, T., Herzog, V.A., Muhar, M., von Haeseler, A., Zuber, J., Ameres, S.L., and Rescheneder, P. (2019). Quantification of experimentally induced nucleotide conversions in high-throughput sequencing datasets. *BMC Bioinformatics* 20, 258. <https://doi.org/10.1186/s12859-019-2849-7>.
98. Jürges, C., Dölken, L., and Erhard, F. (2018). Dissecting newly transcribed and old RNA using GRAND-SLAM. *Bioinformatics* 34, i218–i226. <https://doi.org/10.1093/bioinformatics/bty256>.
99. Erhard, F., Baptista, M.A.P., Krammer, T., Hennig, T., Lange, M., Aramatzki, P., Jürges, C.S., Theis, F.J., Saliba, A.-E., and Dölken, L. (2019). scSLAM-seq reveals core features of transcription dynamics in single cells. *Nature* 571, 419–423. <https://doi.org/10.1038/s41586-019-1369-y>.
100. Rummel, T., Sakellaridi, L., and Erhard, F. (2023). grandR: a comprehensive package for nucleotide conversion RNA-seq data analysis. *Nat. Commun.* 14, 3559. <https://doi.org/10.1038/s41467-023-39163-4>.
101. Olarerin-George, A.O., and Jaffrey, S.R. (2017). MetaPlotR: a Perl/R pipeline for plotting metagenes of nucleotide modifications and other transcriptomic sites. *Bioinformatics* 33, 1563–1564. <https://doi.org/10.1093/bioinformatics/btx002>.
102. Martin, M. (2011). Cutadapt removes adapter sequences from high-throughput sequencing reads. *EMBnet.journal* 17, 10–12. <https://doi.org/10.14806/ej.17.1.200>.
103. Lauria, F., Tebaldi, T., Bernabò, P., Groen, E.J.N., Gillingwater, T.H., and Viero, G. (2018). riboWaltz: Optimization of ribosome P-site positioning in ribosome profiling data. *PLoS Comput. Biol.* 14, e1006169. <https://doi.org/10.1371/journal.pcbi.1006169>.
104. Dobin, A., Davis, C.A., Schlesinger, F., Drenkow, J., Zaleski, C., Jha, S., Batut, P., Chaisson, M., and Gingeras, T.R. (2013). STAR: ultrafast universal RNA-seq aligner. *Bioinformatics* 29, 15–21. <https://doi.org/10.1093/bioinformatics/bts635>.
105. Yu, G., Wang, L.-G., Han, Y., and He, Q.-Y. (2012). clusterProfiler: an R Package for Comparing Biological Themes Among Gene Clusters. *OMICS A J. Integr. Biol.* 16, 284–287. <https://doi.org/10.1089/omi.2011.0118>.
106. Wu, T., Hu, E., Xu, S., Chen, M., Guo, P., Dai, Z., Feng, T., Zhou, L., Tang, W., Zhan, L., et al. (2021). clusterProfiler 4.0: A universal enrichment tool for interpreting omics data. *Innovation (Camb)* 2, 100141. <https://doi.org/10.1016/j.xinn.2021.100141>.
107. Shah, A., Qian, Y., Weyn-Vanhentenryck, S.M., and Zhang, C. (2017). CLIP Tool Kit (CTK): a flexible and robust pipeline to analyze CLIP sequencing data. *Bioinformatics* 33, 566–567. <https://doi.org/10.1093/bioinformatics/btw653>.
108. Krueger, F., James, F., Ewels, P., Afyounian, E., Weinstein, M., Schuster-Boeckler, B., Hulselmans, G., and sclamons. (2023). FelixKrueger/Trim-Galore: v0.6.10 - add default decompression path (Zenodo) <https://doi.org/10.5281/zenodo.7598955>.
109. Patro, R., Duggal, G., Love, M.I., Irizarry, R.A., and Kingsford, C. (2017). Salmon provides fast and bias-aware quantification of transcript expression. *Nat. Methods* 14, 417–419. <https://doi.org/10.1038/nmeth.4197>.
110. Soneson, C., Love, M.I., and Robinson, M.D. (2015). Differential analyses for RNA-seq: transcript-level estimates improve gene-level inferences. *F1000Res* 4, 1521. <https://doi.org/10.12688/f1000research.7563.2>.
111. Schofield, J.A., Duffy, E.E., Kiefer, L., Sullivan, M.C., and Simon, M.D. (2018). TimeLapse-seq: adding a temporal dimension to RNA sequencing through nucleoside recoding. *Nat. Methods* 15, 221–225. <https://doi.org/10.1038/nmeth.4582>.
112. Kumari, R., Michel, A.M., and Baranov, P.V. (2018). PausePred and Rfeet: webtools for inferring ribosome pauses and visualizing footprint density from ribosome profiling data. *RNA* 24, 1297–1304. <https://doi.org/10.1261/rna.065235.117>.
113. Chen, E.Y., Tan, C.M., Kou, Y., Duan, Q., Wang, Z., Meirelles, G.V., Clark, N.R., and Ma'ayan, A. (2013). Enrichr: interactive and collaborative HTML5 gene list enrichment analysis tool. *BMC Bioinformatics* 14, 128. <https://doi.org/10.1186/1471-2105-14-128>.
114. Kuleshov, M.V., Jones, M.R., Rouillard, A.D., Fernandez, N.F., Duan, Q., Wang, Z., Koplev, S., Jenkins, S.L., Jagodnik, K.M., Lachmann, A., et al. (2016). Enrichr: a comprehensive gene set enrichment analysis web server 2016 update. *Nucleic Acids Res.* 44, W90–W97. <https://doi.org/10.1093/nar/gkw377>.
115. Clarke, D.J.B., Jeon, M., Stein, D.J., Moiseyev, N., Kropiwnicki, E., Dai, C., Xie, Z., Wojciechowicz, M.L., Litz, S., Hom, J., et al. (2021). Appyters: Turning Jupyter Notebooks into data-driven web apps. *Patterns (N Y)* 2, 100213. <https://doi.org/10.1016/j.patter.2021.100213>.
116. Pagès, H., Carlson, M., Falcon, S., and Li, N. (2023). AnnotationDbi: Manipulation of SQLite-based annotations in Bioconductor. Version 1.64.1 (Bioconductor version: Release (3.18)). <https://doi.org/10.18129/B9.bioc.AnnotationDbi>.
117. Shimada, K., Bachman, J.A., Muhlich, J.L., and Mitchison, T.J. (2021). shinyDepMap, a tool to identify targetable cancer genes and their functional connections from Cancer Dependency Map data. *eLife* 10, e57116. <https://doi.org/10.7554/eLife.57116>.
118. van Hoof, A., Frischmeyer, P.A., Dietz, H.C., and Parker, R. (2002). Exosome-Mediated Recognition and Degradation of mRNAs Lacking a Termination Codon. *Science* 295, 2262–2264. <https://doi.org/10.1126/science.1067272>.
119. Karanasios, E., Stapleton, E., Manifava, M., Kaizuka, T., Mizushima, N., Walker, S.A., and Ktistakis, N.T. (2013). Dynamic association of the ULK1 complex with omegasomes during autophagy induction. *J. Cell Sci.* 126, 5224–5238. <https://doi.org/10.1242/jcs.132415>.

STAR★METHODS

KEY RESOURCES TABLE

REAGENT or RESOURCE	SOURCE	IDENTIFIER
Antibodies		
anti-pan-YTHDF antibody	Cell Signaling	41437; RRID: AB_3668993
anti-METTL3 rabbit polyclonal antibody	ProteinTech	15073-1-AP; RRID: AB_2142033
anti-GAPDH rabbit monoclonal antibody	Cell Signaling	5174S; RRID:AB_10622025
anti-puromycin mouse monoclonal antibody	ThermoFisher	MABE343; RRID:AB_2566826
anti-eIF2 α rabbit monoclonal antibody	Cell Signaling	5324; RRID:AB_10692650
anti-eIF2 α S51phospho-specific rabbit monoclonal antibody	Cell Signaling	3398; RRID:AB_2096481
anti-H3 rabbit polyclonal antibody	Abcam	ab1791; RRID:AB_302613
anti-RPS6 rabbit monoclonal antibody	Cell Signaling	2217; RRID:AB_331355
anti-ATG12 rabbit monoclonal antibody	Cell Signaling	4180; RRID:AB_1903898
anti-ULK1 rabbit monoclonal antibody	Cell Signaling	8054; RRID:AB_11178668
Alexa Fluor 488-conjugated anti-rabbit IgG antibody	ThermoFisher	A21206; RRID:AB_2535792
Chemicals, peptides, and recombinant proteins		
RNaseA	NEB	T3018L
Deposited data		
m6A mapping (GLORI) in MEF	Liu et al. ³⁷	GEO: GSE210563
m6A mapping (GLORI) in HeLa	Liu et al. ³⁷	GEO: GSE210563
m6A mapping (GLORI) in mESC	Liu et al. ³⁷	GEO: GSE210563
m6A mapping (miCLIP) in MEF	Boulias et al. ³⁶	GEO: GSE122948
m6A mapping (miCLIP) in mESC	Ke et al. ⁹¹	GEO: GSE86336
Gene expression, YTHDF1/2/3 triple knockdown in HeLa	Zaccara et al. ¹⁰	GEO: GSE134380
Gene expression, puromycin treatment in Flip-In HEK293	Fritz et al. ⁴¹	GEO: GSE162699
Gene expression, amino acid depletion in MEF	Kim et al. ⁶⁹	GEO: GSE199923
Gene expression, amino acid and serum depletion in MEF	Goldsmith et al. ⁷⁰	ENA: PRJNA634689
Gene expression, amino acid and serum depletion in Hap1	Peeters et al. ⁷¹	GEO: GSE107600
Gene expression, tunicamycin treatment in U2OS	Wang et al. ⁷⁵	GEO: GSE30499
Gene expression, tunicamycin treatment in MEF	Torrence et al. ⁷⁴	GEO: GSE158605
Gene expression, ASCC3 knockdown in HEK293T	Kito et al. ⁵⁶	GEO: GSE186502
Gene expression, STM2457 treatment in HEK293T	Rücklé et al. ⁴⁷	GEO: GSE203642
Disome profiling, HEK293	Han et al. ⁵²	GEO: GSE133393
Monosome/disome profiling, HEK293T	Ferguson et al. ⁴⁴	ENA: SRP419255
YTHDF1/2/3 and YTHDC1 iCLIP, HEK293T	Patil et al. ⁶³	GEO: GSE78030
TimeLapse-seq, emetine treatment in mESC	This study	GEO: GSE248503

(Continued on next page)

Continued

REAGENT or RESOURCE	SOURCE	IDENTIFIER
TimeLapse-seq, <i>YTHDF1/2/3</i> triple knockdown in HeLa	This study	GEO: GSE248503
TimeLapse-seq, amino acid depletion in <i>Mettl3</i> knockout MEF	This study	GEO: GSE248503
Monosome profiling, <i>Mettl14</i> knockout mESC	This study	GEO: GSE248503
Disome structure	Juszkiewicz et al. ⁵⁰	PDB: 6HCM, 6HCQ
Experimental models: Cell lines		
Mouse embryonic stem cell	Geula et al. ²	N/A
Mouse embryonic fibroblast	Ries et al. ⁹² and this study	N/A
Human female origin: HeLa cells	ATCC	CCL-2; RRID:CVCL_0030
Software and algorithms		
DESeq2 v1.34.0	Love et al. ⁹³	https://bioconductor.org/packages/release/bioc/html/DESeq2.html
R v4.1.2	R Core Team ⁹⁴	https://cran.r-project.org/
R v4.3.0.	R Core Team ⁹⁴	https://cran.r-project.org/
MultiQC 1.14	Ewels et al. ⁹⁵	https://github.com/MultiQC/MultiQC
TrimGalore-0.6.9	Simon ⁹⁶	https://github.com/FelixKrueger/TrimGalore
SLAM-DUNK 0.4.3	Neumann et al. ⁹⁷	https://t-neumann.github.io/slamdunk/
GRAND-SLAM 2.0.7b	Jürges et al. ⁹⁸ ; Erhard et al. ⁹⁹	https://erhard-lab.de/software
grandR 0.2.2	Rummel et al. ¹⁰⁰	https://github.com/erhard-lab/grandR
MetaPlotR	Olarerin-George et al. ¹⁰¹	https://github.com/olarerin/metaPlotR
cutadapt v4.1	Martin ¹⁰²	https://cutadapt.readthedocs.io/en/v4.1/index.html#
riboWaltz v2.0	Lauria et al. ¹⁰³	https://github.com/LabTranslationalArchitectomics/riboWaltz#citing-ribowaltz
STAR 2.7.9a	Dobin et al. ¹⁰⁴	https://github.com/alexdobin/STAR
clusterProfiler 4.8.1	Yu et al. ¹⁰⁵ ; Wu et al. ¹⁰⁶	https://guangchuangyu.github.io/software/clusterProfiler/
CTK v1.1.3	Shah et al. ¹⁰⁷	https://zhanglab.c2b2.columbia.edu/index.php/CTK_Documentation
Experimental models: Cell lines		
si <i>YTHDF1/2/3</i>	Zaccara et al. ¹⁰	N/A

EXPERIMENTAL MODEL AND STUDY PARTICIPANT DETAILS

Cell culture

Mettl3^{flox/flox} MEFs⁹² of unknown sex were grown at 37°C in 5% CO₂ using DMEM (ThermoFisher, 11995065) supplemented with 10% FBS and 10 U/mL penicillin-streptomycin (ThermoFisher, 15140122). Cells were passaged every 3–4 days using TrypLE Express (ThermoFisher, 12604039) according to the manufacturer's instructions. Cells were then transduced with the Cre-ERT2 lentivirus and selected by hygromycin treatment. To conditionally deplete *Mettl3* in MEFs, *Mettl3*^{flox/flox} MEFs expressing Cre-ERT2 were treated with 500 nM 4-hydroxytamoxifen for 10 days before experiments.

mESCs, generated from a male mouse embryo, were a gift from J. Hanna and S. Geula (Weizmann Institute of Science).² mESCs were grown in KnockOut DMEM (ThermoFisher, 10829018) supplemented with 15% heat-inactivated FBS, 10 U/mL Penicillin-Streptomycin (ThermoFisher, 15140122), 1x GlutaMax (ThermoFisher, 35050061), 500 μM β-mercaptoethanol (ThermoFisher, 21985023), 1x Nonessential amino acids (ThermoFisher, 11140076), 10³ U/mL LIF (MilliporeSigma, ESG1107), 3 μM CHIR99021 (ThermoFisher, 501013679), and 1 μM PD0325901 (ThermoFisher, 501013147).² Cells were plated on plates coated with Embryo-Max™ 0.1% gelatin solution (MilliporeSigma, ES-006-B) and passaged daily using TrypLE Express (ThermoFisher, 12604039) according to the manufacturer's instructions.

HeLa (ThermoFisher, 50-238-3230) were grown at 37°C in 5% CO₂ using DMEM (ThermoFisher, 11995065) supplemented with 10% FBS and 10 U/mL penicillin-streptomycin (ThermoFisher, 15140122). Cells were passaged every 3-4 days using with TrypLE Express (ThermoFisuer, 12604039) according to the manufacturer's instructions.

To deplete amino acids, cells were washed with PBS (ThermoFisher, 10010049) three times, then the PBS was replaced with amino acid-replete or amino acid-depleted media for 3 h. Amino acid-replete media was prepared using DMEM (US Biological, D9800) supplemented with 3.5 g/L glucose, 3.7g/L sodium bicarbonate, and 10% dialyzed FBS (ThermoFisher A3382001). The amino acid composition of this DMEM is: L-Arginine-HCl (0.084 g/L, 398.7 μM), L-Cystine-2HCl (0.0626 g/L, 199.9 μM), L-Glutamine (0.584 g/L, 4.0 mM), Glycine (0.03 g/L, 399.6 μM), L-Histidine-HCl-H₂O (0.042 g/L, 200.4 μM), L-Isoleucine (0.105 g/L, 800.5 μM), L-Leucine (0.105 g/L, 800.5 μM), L-Lysine-HCl (0.146 g/L, 998.7 μM), L-Methionine (0.03 g/L, 201.1 μM), L-Phenylalanine (0.066 g/L, 399.5 μM), L-Serine (0.042 g/L, 399.7 μM), L-Threonine (0.095 g/L, 797.5 μM), L-Tryptophan (0.016 g/L, 78.3 μM), L-Tyrosine-2Na·2H₂O (0.10379 g/L, 397.3 μM), L-Valine (0.094 g/L, 802.3 μM). Amino acid-depleted media was prepared using amino acid-free DMEM (US Biological, D9800-13) supplemented with 3.5 g/L glucose, 3.7 g/L sodium bicarbonate, 1 mM sodium pyruvate, and 10% dialyzed FBS (ThermoFisher, A3382001).

Translation levels were determined by labeling nascent peptide with puromycin (100 μg/mL) for 10 min after treating cells with amino acid replete or amino acid depleted media.

METHOD DETAILS

Antibodies

For immunoblotting experiments, we used anti-pan-YTHDF antibody (Cell Signaling, 41437T), anti-METTL3 rabbit polyclonal antibody (ProteinTech, 15073-1-AP), anti-GAPDH rabbit monoclonal antibody (Cell Signaling, 5174S), anti-puromycin mouse monoclonal antibody (ThermoFisher, MABE343MI), anti-eIF2α rabbit monoclonal antibody (Cell Signaling, 5324T), anti-eIF2α S51phospho-specific rabbit monoclonal antibody (Cell Signaling, 3398T), anti-H3 rabbit polyclonal antibody (Abcam, ab1791), anti-RPS6 rabbit monoclonal antibody (Cell Signaling, 2217T), as primary antibodies. We used HRP-conjugated anti-rabbit IgG antibody (VWR, 95017-556) as a secondary antibody.

For immunostaining experiments, we used anti-ATG12 rabbit monoclonal antibody (Cell Signaling, 4180T) and anti-ULK1 rabbit monoclonal antibody (Cell Signaling, 8054T) as primary antibodies. We used Alexa Fluor 488-conjugated anti-rabbit IgG antibody (Life Technologies, A21206) as a secondary antibody.

Reporter construct cloning

CDS or 3' UTR m⁶A reporters were cloned in the pcDNA™3.1 (+) (ThermoFisher, V79020) vector. The plasmid was first modified by replacing the Neomycin resistance gene with an mCherry gene containing DRACH mutations. In this mCherry gene, prepared as a gBlock (IDT), every m⁶A consensus DRACH motif was mutated using synonymous codons. The mCherry gBlock was cloned using NEBuilder® HiFi DNA Assembly Master Mix (NEB, E2621L) into a plasmid digested with XmaI and BstBI. To create the CDS reporter, synthetic DNA fragments encoding the endogenous promoters and the gene bodies were cloned into the plasmid to replace the CMV promoter and the multiple cloning site. In these synthetic DNA fragments, a few nucleotides outside of the DRACH motifs were mutated to ensure selective amplification of the reporter but not the endogenous transcript during qPCR. To create the 3' UTR reporter, one or two nucleotides were mutated to introduce a stop codon upstream of the first DRACH motif in the CDS using Q5 DNA polymerase (NEB, M0492S).

For the m⁶A-codon reporters, pcDNA™3.1 (+) containing the DRACH-mutant mCherry in place of the Neomycin resistance gene described above was used. The SD40 tag and a NanoLuc luciferase gene were cloned into the multiple cloning site under the CMV promoter. All DRACH motifs in the SD40-tag and NanoLuc luciferase gene were mutated using synonymous codons. Next, we cloned a synthetic DNA fragment containing a cluster of 21 repeats of one of nine m⁶A-containing codons, each codon derived from endogenous m⁶A-mRNAs. In these reporters, the SD40 tag, an m⁶A-containing codon cluster, and the NanoLuc luciferase gene were cloned in-frame.

Transfection of reporter genes

Cells were seeded in 12-well plates immediately prior to transfection. 500 ng plasmid was transfected to each well using FuGene HD transfection reagent (Promega, E2311) according to the manufacturer's instruction. 48 h after transfection, cells were treated with or without 10 μg/mL actinomycin D for 3 h. mRNA was harvested at 0 and 3 h to measure the stability. This early time point was used since m⁶A-containing mRNAs typically have short half-lives.

Western blotting

Cells were lysed in lysis buffer [20 mM HEPES, pH 7.9, with 1.5 mM MgCl₂, 0.42 M NaCl, 0.5% NP-40, 0.2 mM EDTA, 25% (v/v) glycerol, 1 mM DTT, 1x protease inhibitor cocktail (ThermoFisher, 1861279)] on a vortex at 4°C for 15 min. Lysate was cleared by spinning at 4°C at 21,000 × g for 20 min and quantified by Bradford assay (Bio-Rad, 5000006). 15 μg cell lysate was run on each lane on a NuPage 4-12% Bis-Tris pre-cast gel (ThermoFisher, NP0323BOX) and then transferred to a PVDF membrane (MilliporeSigma, IPVH00010). The membrane was blocked with 5% milk and blotted overnight at 4°C with the indicated primary antibodies in 5%

BSA. HRP-conjugated anti-rabbit IgG antibody was used as a secondary antibody in 5% milk for 1 h at room temperature. Immunoblots were developed using Amersham ECL Western Blotting Detection Reagent (Cytiva, RPN2209) on a Bio-Rad ChemiDoc Imaging system.

Coimmunoprecipitation of YTHDF2

mESC grown to 80% confluence were washed with ice-cold PBS twice, then lysed in 800 µL lysis buffer [20 mM Tris-HCl, pH 7.4, 150 mM NaCl, and 0.5% NP-40, 1x protease inhibitor cocktail (ThermoFisher, 1861279)]. After 5 min incubation on ice, the nuclei were removed by spinning at 4°C at 500 × g for 5 min. The supernatant was transferred to a new tube, and protein concentration was measured. 500 µg of total protein was prepared in 1 mL lysis buffer. 10 µg RNaseA (NEB, T3018L) was added to the lysate and incubated for 30 min at 4°C. 5% lysate was set aside as input. 4 µg YTHDF2 antibody captured on Dynabeads protein A (ThermoFisher, 10002D) was added to the rest of the lysate and incubated for 2 h at 4°C. After immunoprecipitation, the beads were washed once with high salt buffer [20 mM Tris-HCl, pH 7.4, 300 mM NaCl, 0.5% NP-40, 1x protease inhibitor cocktail (ThermoFisher, 1861279)] and then twice with lysis buffer. After the last wash, beads were resuspended in 1x SDS loading dye for Western blotting.

RT-qPCR

Total RNA was isolated from cells using Trizol reagent (ThermoFisher, 10296010) according to the manufacturer's instructions. 500 ng of RNA was treated with DNasel (ThermoFisher, EN0521) and subjected to reverse transcription with oligo-dT primers using SuperScript IV (ThermoFisher, 18090200). cDNA was used for qPCR using PowerUp™ SYBR™ Green Master Mix (ThermoFisher, A25742) in a ThermoFisher QuantStudio5 Real-Time PCR System. Continuous melting temperature was measured after PCR amplification to ensure the amplification specificity. A pooled cDNA mix was used to prepare a standard curve for each primer set. The average of Ct values from two technical replicates were used to calculate the relative expression levels using the standard curve for each primer set. Expression levels were normalized by a control non-m⁶A gene (*Polr3h*) expression. Primer sequences are listed in [Table S5](#).

Reanalysis of previously published RNA-seq dataset

We used the processed data deposited under each accession number for previously published RNA-seq datasets ([key resources table](#)). We used the results from differential gene expression analysis when available within data under the accession number. When the count tables are provided without differential expression analysis, we analyzed differential gene expression using DEseq2 v1.34.0 with the default parameters.⁹³ When read counts are not provided, the library quality was first assessed using FastQC,⁹⁶ followed by adapter trimming with TrimGalore,¹⁰⁸ and another round of quality control using FastQC.⁹⁶ The pre-processed reads were quantified using Salmon¹⁰⁹ and summarized at gene-level using tximport package¹¹⁰ for the subsequent differential gene expression analysis using DEseq2 v1.34.0 with the default parameters.⁹³ Further computation and plotting were performed using a custom script on R v4.1.2.⁹⁴

siRNA-mediated YTHDF1/2/3 knockdown

We used 10 nM siRNA targeting each of the YTHDF1, YTHDF2, and YTHDF3 mRNAs to achieve effective triple knockdown.¹⁰ As a control, 30 nM non-targeting siRNA (IDT, 51-01-14-03) was used. The siRNAs were transfected into 0.5×10^6 HeLa cells seeded in a 6-well plate. 24 h after the first transfection, cells were transfected again. 48 h after the first transfection, cells were trypsinized and replaced in a 6-well plate for western blotting and 12-well plate for mRNA half-life measurement.

TimeLapse-seq library preparation and sequencing

TimeLap-seq was performed as previously described.¹¹¹ Briefly, cells were grown to 80% confluence. To determine the effect on translation on mRNA stability in mESC, cells were treated with 200 µM emetine with 250 µM 4-thiouridine for 3 h. For the similar experiment in HeLa, cells were treated with 200 µM emetine with 500 µM 4-thiouridine for 1.5 h. To determine the effects of amino acid depletion, MEFs were washed with PBS for three times, and then incubated in amino acid replete or amino acid-depleted media for 3 h with 500 µM 4-thiouridine (4sU, SigmaAldrich, T4509). Total RNA was collected using Qiagen RNeasy Mini kit RLT buffer (Qia- gen, 74104) supplemented with 1% β-mercaptoethanol (BME). Cells were lysed by passing through a 25-gauge needle, and RNA was isolated following the manufacturer's instruction with RPE buffer supplemented with 1% BME. 10 µg total RNA was treated with 2,2,2-trifluoroethylamine (TFEE) and sodium periodate (NaIO₄) at 45 °C for 1 h to convert 4sU to N⁴-trifluoroethylcytosine. RNA was then purified twice using RNAClean beads (Beckman Coulter, A63987). 1 µg of treated RNA was used for RNA-seq library preparation using NEBNext® rRNA Depletion Kit (NEB, E6310X) and NEBNext® Ultra™ II Directional RNA Library Prep Kit (NEB, E7760L). Library quality was assessed on Agilent TapeStation4200 using D1000 ScreenTape (Agilent, 5067-5582). Library was quantified on Qubit4 Fluorometer using Qubit 1X dsDNA HS Assay Kit (ThermoFisher, Q33231). Libraries were sequenced with pair-end 2x100 cycles on Illumina NovaSeq 6000.

TimeLapse-seq library data analysis

Library quality was first analyzed using MultiQC 1.14.⁹⁵ Adapters were trimmed using TrimGalore-0.6.9¹⁰⁸ with –stringency 3 and library quality was again assessed using MultiQC 1.14.⁹⁵ The data was then analyzed using the slambdunk all function of the analytical

suite SLAM-DUNK 0.4.3 with the default parameters for mapping, quality filtering, and single nucleotide polymorphism identification.⁹⁷ The reference genome hg38 and mm10 was used for mapping and the subsequent analysis. PCR duplicates in the quality filtered reads were collapsed using alleoop collapse function of SLAM-DUNK 0.4.3. The 4sU conversion was further assessed using alleoop rates, alleoop tccontext, and alleoop snpeval functions with the default parameters. alleoop utrrates was used with a bed file of all exons of each mRNA to analyzed 4sU conversion rates per mRNA. The quality filtered and PCR duplicate-collapsed mapped reads were further analyzed using GRAND-SLAM 2.0.7b^{98,99} with the default parameters to quantify read counts and perform statistical analysis to infer the ratio of transcripts for each gene that originate from pre-4sU labeling and post labeling. The results from GRAND-SLAM 2.0.7b was used to calculate mRNA synthesis rate and half-life using grandR 0.2.2.¹⁰⁰ Further computation and plotting were performed using a custom script on R v4.1.2.⁹⁴

m⁶A quantification

We used the processed data deposited under each accession number for previously published GLORI and miCLIP datasets (see [key resources table](#)). The mapped m⁶A sites in the chromosome coordinates were first converted to the transcriptome coordinates using MetaPlotR.¹⁰¹ The longest transcript for each gene was selected for the further analysis. For the GLORI dataset, the stoichiometry for each m⁶A site was appended to each m⁶A site at each transcriptome coordinate. Cumulative m⁶A amounts for 5' UTR, CDS, 3' UTR, and the entire transcript for each gene was calculated based on the output from MetaPlotR¹⁰¹ using a custom script on R v4.1.2.⁹⁴ It should be noted that our m⁶A calling likely underestimates the ground truth of m⁶A amount. When calling m⁶A sites using methods such as GLORI, m⁶A stoichiometries cannot be calculated over some regions due to insufficient read coverage. Our analysis designates these sites as non-methylated. Additionally, m⁶A sites below the 5% stoichiometry threshold are designated as non-methylated to avoid false positive calls of m⁶A sites.

In [Figures 2H](#) (right), [4B](#) (right), and [S3B](#) (right), we quantified m⁶A levels in the 5' UTR, CDS, and 3' UTR by summing the m⁶A stoichiometries of each mapped m⁶A site using a sliding window measuring 500 transcripts.

Library preparation of OTTR ribosome profiling

OTTR ribosome profiling was performed as previously described⁴⁴ using OTTR cDNA library construction kit (Karnateq, R2201001S). Briefly, cells were grown in a 150 mm dish to 70% confluence. Cells were washed with ice-cold PBS supplemented with 100 µg/mL cycloheximide and 100 µg/mL tigecycline. Cells were lysed in 300 µL lysis buffer [20 mM Tris-HCl, pH 7.4, 150 mM NaCl, 5 mM, MgCl₂, 1 mM DTT, 1 % Triton X, 100 µg/mL cycloheximide, 100 µg/mL tigecycline, and 15 U/mL DNase I (ThermoFisher, 89836)]. Lysates were passed through a 25-gauge needle five times, incubated on ice for 20 min, and clarified by centrifugation for 10 min at 20,000 x g at 4 °C. RNA in the lysate was quantified using Qubit™ RNA Broad Range kit (ThermoFisher, Q10211) on Qubit4 Fluorometer. 30 µg RNA was digested using 600 U P1 nuclease (NEB, M0660S) in 400 µL supplemented with 42 µL 0.2 M Bis-Tris, pH 6.0 (Life Technologies, J62686.AE) at 37 °C for 1 h. OTTR ribosome profiling libraries were prepared using mirRICH small RNA enrichment method according to the manufacturer's instruction. Final library quality was assessed on Agilent TapeStation4200 using D1000 ScreenTape (Agilent, 5067-5582). Library was quantified on Qubit4 Fluorometer using Qubit 1X dsDNA HS Assay Kit (ThermoFisher, Q33231). Libraries were sequenced with single-end 100 cycles on Illumina NovaSeq 6000.

Analysis of OTTR monosome profiling

OTTR monosome profiling dataset was processed as previously described.⁴⁴ Briefly, the adaptor was trimmed and the unique molecular identifier and a single nucleotide at the beginning of the sequencing introduced during OTTR library preparation method were removed from the sequencing reads using cutadapt v4.1.¹⁰² Sequencing reads were further filtered for minimal 20 bp and quality score 10 using cutadapt v4.1.¹⁰² The pre-processed reads were first aligned to ribosomal RNAs. Reads that did not align to ribosomal RNAs were then aligned to the transcriptome in which a single transcript with the longest CDS was selected for each protein coding gene. Alignment to the transcriptome was performed using the following parameters: -sjdbOverhang 43 –alignSjoverhangMin 1 –alignSJDBoverhangMin 1 –seedSearchStartLmax 20 –outFilterMultimapNmax 1 –outFilterMismatchNmax 2 –alignEndsType End-ToEnd. Aligned reads were further analyzed using riboWaltz v2.0. For the libraries generated with RNase I, the aligned reads were filtered for the length of 28-31 bp, while the length filter of 32-38 bp was applied to the libraries generated using P1 nuclease. Offset to the A-site was determined using riboWaltz psite function with the default parameters. The mapped A-site was further analyzed using custom scripts in R v4.1.2.²⁶

For determining ribosome stalling index, CDS m⁶A that are > 120 nt from the start and stop codons were used to avoid the stalled ribosome at the start and stop codons. To determine ribosome stalling, the total number of A-sites within +/- 30 or 45 nucleotide window from the first nucleotide of each m⁶A-containing codon was quantified. m⁶A sites that have at least 10 A-site counts within this window were filtered for further analysis. We used two methods to define stalling index as follows. In the first method, referred to as the mean rescaled A-site count method, A-site counts for each nucleotide position within the window around each m⁶A site were normalized by the mean A-site counts of all nucleotide positions within the same window. The stalling index was then defined as the mean of these rescaled A-site counts at each nucleotide position within the window across all m⁶A sites. In the second method, referred to as the z-score method, A-site counts at each nucleotide position within the window around each m⁶A site were transformed to z-scores using the mean and standard deviation of A-site counts of all nucleotide positions within the same window.

The stalling index was calculated as the mean z-score at each nucleotide position within the window across all m⁶A sites.^{4,5} The z-score helps to adjust for variability in read coverage in lower-expressed mRNAs or lowly translated mRNAs.¹¹²

The monosome profiling dataset generated with RNaseI (SRA accession number: SAMN32928155, SAMN32928156) was used in Figures 2A–2D, S2C, S2D, and S2G, and the dataset generated with P1 nuclease (SRA accession number: SAMN32928153, SAMN32928154) was used in Figure 3D.

Analysis of OTTR disome profiling

OTTR disome profiling dataset generated using P1 nuclease was processed as previously described.⁴⁴ Briefly, the adaptor was trimmed using cutadapt v4.1.¹⁰² PCR duplicates were collapsed using CTK v1.1.3 fastq2collapse.pl script.¹⁰⁷ The unique molecular identifier and a single nucleotide at the beginning of the sequencing introduced during OTTR library preparation method were removed from the sequencing reads using cutadapt v4.1.¹⁰² Sequencing reads were further filtered for minimal 20 bp and quality score 10 using cutadapt v4.1.¹⁰² The pre-processed reads were first aligned to ribosomal RNAs using STAR 2.7.9a.¹⁰⁴ Reads that did not align to ribosomal RNAs were then aligned to the transcriptome in which a single transcript with the longest CDS was selected for each protein coding gene. Alignment to the transcriptome was performed using the following parameters: –sjdbOverhang 51 –alignSjOverhangMin 1 –alignSJDBoverhangMin 1 –seedSearchStartLmax 20 –outFilterMultimapNmax 8 –outFilterMismatchNmax 2. Aligned bam files were further analyzed using riboWaltz v2.0 and custom scripts in R v4.1.2.²⁶

To quantify the 5' and 3' extremities of disome footprints in the vicinity of m⁶A, the aligned reads were first filtered for the length of 42–72 bp. The 5' and 3' extremities at each nucleotide position within the indicated range from the first nucleotide of m⁶A-containing codon was counted for each m⁶A site. m⁶A sites that have at least 10 counts of each extremity within the indicated window were filtered for further analysis. For each m⁶A site, the z-score of the 5' and 3' extremity count was calculated for each nucleotide position within the window for each m⁶A site and the mean z-score for all m⁶A sites of interest was used for quantification and plotting. Background disome footprints were quantified as 5' and 3' extremities around non-methylated sequence-matched control codons. For this analysis, CDS m⁶A or the control non-methylated codons that are >120 nt from the start and stop codons were used to avoid the stalled ribosomes at the start and stop codons.

To quantify collided disomes associated with each m⁶A, disome footprints were first filtered for 51–61 nt length. Disome footprints whose 5' and 3' extremities are located at 44–54 nt upstream and 4–8 nt downstream relative to the first nucleotide of the m⁶A-containing codons, respectively, were counted as disome associated with the respective m⁶A.

The disome profiling dataset generated with P1 nuclease (SRA accession number: SAMN32928159, SAMN32928160) was used in Figures 3B, 4C, and S4B.

Analysis of YTHDF iCLIP datasets

YTHDF1/2/3 iCLIP coverage at each m⁶A site was obtained from a previous study. To define m⁶A with and without associated disomes, we first mapped disome footprints around each m⁶A site. For all disome mapping below, disome footprints were first filtered for 51–61 nt length.

To determine m⁶A sites with associated disomes, we filtered for m⁶A sites that have the 5' and 3' disome footprint extremities located 44–54 nt upstream and 4–8 nt downstream relative to the first nucleotide of the m⁶A-containing codons, respectively. Only m⁶A located >120 nt from the start and stop codons are used in this analysis. We then filtered for CDS m⁶A that have at least one mapped associated disome(s).

To determine m⁶A sites without associated disomes, we first filtered for the set of transcripts that have m⁶A sites with at least one associated disome(s) to control for gene expression and translation levels. We then filtered for CDS m⁶A that are > 120 nt from the start and stop codons and that have no associated disomes. To normalize for m⁶A stoichiometry between two groups of m⁶A, we grouped m⁶A with associated disomes into bins of 5% increment based the stoichiometry. The control m⁶A group was randomly sampled from the no-disome-associated m⁶A sites in order to match to the disome-associated m⁶A sites for (1) the median m⁶A stoichiometry, (2) the upper and lower limit of m⁶A stoichiometry, and (3) the overall distribution of m⁶A stoichiometries, (i.e., frequency of sites in each m⁶A stoichiometry bin using 5% increments).

Analysis of Toxicogenomic Project database

A list of highly methylated genes was prepared by selecting genes with more than 5 detected m⁶A sites in miCLIP dataset in MEF³⁶ (Table S2). The TG-GATES Toxicogenomic Project database screen for highly methylated genes was performed on the webtool Enricher (<https://maayanlab.cloud/Enrichr/>).^{113,114} In this screen, the odds ratio of the highly methylated genes and the genes whose expression was altered by the treatment was computed for each compound. The odds ratio and the associated p-value for each compound were retrieved as screening results and provided to the webtool Appyter (<https://appyters.maayanlab.cloud/#/>) for plotting.¹¹⁵

DepMap co-dependency screen

Top 100 co-dependency genes and their dependency scores with METTL3 knockout were downloaded from DepMap (<https://depmap.org/portal/>, 23Q2+Score Chronos dataset). Each subunit of the m⁶A writer complex was annotated using a manually curated list of all subunits.¹¹ Lists of genes related to the ribosomes, translation, and tRNA biogenesis pathways were retrieved using

the Bioconductor annotation package¹¹⁶ using GO IDs in Table S3. Among the top 100 co-dependent genes with METTL3, genes with positive dependency scores were plotted using R v4.1.2.⁹⁴

Immunofluorescence

Cells were seeded on an 8-well glass-bottom chamber slide (VWR, 62407-296) coated with EmbryoMax 0.1% Gelatin Solution (MilliporeSigma, ES-006-B). 48 h after seeding, cells were washed three times with PBS and the media was replaced with amino acid replete or amino acid-depleted media for 3 h. Cells were then fixed in 4% formaldehyde (ThermoFisher, 28906) for 10 min at room temperature, and permeabilized in 0.2% Triton-X. After blocking with 5% FBS, cells were stained with primary antibodies at 4°C for overnight in 5% FBS. After washing cells three times with PBS supplemented with 0.1% Tween-20, cells were stained with a secondary antibody in 5% FBS for 1 h at room temperature. After washing the cells three times with PBS supplemented with 0.1% Tween-20, cells were mounted using mounting solution containing DAPI (ThermoFisher, P36961). After antibody staining, images were acquired using a Nikon TE-2000 inverted microscope with a 40x oil objective. All images for a given antibody in each imaging session was used an identical exposure time that ensured that pixels were not saturated. Shown in Figures 5D and S6F are representative composite images of an autophagy marker (i.e. ATG12 or ULK1).

Immunostained puncta was analyzed using the FIJI distribution of ImageJ2 (v1.14.0/1.54f). Puncta was detected by subtracting the two copies of the original image filtered through Gaussian blur with sigma value set to 1.00 and 2.00 for each copy. Gaussian blurred image with sigma value 2.00 was subtracted from the blurred image with sigma value 1.00. Puncta was identified using threshold on the subtracted image, and the size of each punctum was measured using set measurement function.

In vitro ribosome collision assay

To setup an *in vitro* system to visualize monosome and collided ribosome footprints, mRNA was prepared using α-[³²P]-CTP and 3'-O-Me-m7G(5')ppp(5')G RNA Cap Structure Analog (NEB, S1411L) along with cold ATP, UTP, CTP, and GTP using HiScribe T7 High Yield RNA Synthesis Kit (New England Biolabs, E2040S). The synthesized mRNA was purified using 1x volume of RNAClean XP beads (Beckman, A63987) according to the manufacturer's instruction and quantified using Qubit Broad RNA Assay Kit (ThermoFisher, Q10211). The purified mRNA was used for *in vitro* translation in HeLa lysate (ThermoFisher, 88882) for 25 min at 30°C. To induce ribosome collisions, low dose emetine (0.5 μM) was also included in the translation reaction. 200 μM emetine treatment, which prevents ribosome collisions, was used in another *in vitro* translation reaction to generate a monosome standard. At the end of the experiment, we stopped the reaction by adding 200 μM emetine. The reaction lysate was subjected to partial digestion using Micrococcal nuclease (400 activity unit; ThermoFisher, 88216) in the presence of 15 mM CaCl₂ for 45 min at room temperature to obtain ribosome footprints. Ribosome footprints were purified using TRIzol according to the manufacturer's instruction and ran on 10% TBE-urea gel followed by transferring to a nylon membrane for autoradiography. Radioactive signals were visualized using an Amersham Typhoon 5 (Firmware v303, software v2.0.0.6). To confirm that the appearance of ribosome footprints is translation dependent, each reaction was carried out with or without the addition of 0.5 μM recombinant eIF4E.

To test if m⁶A can induce ribosome collision *in vitro*, a new set of α-[³²P]-CTP labeled mRNAs were prepared using *in vitro* transcription as described above but using either ATP (for A-mRNA) or m⁶ATP (for m⁶A-mRNA; Jena Bioscience, NU-1101S). These mRNAs consist of N-terminal 125-nt region without A except at the start codon followed by a C-terminal 41-nt region that contains either 17 A's or m⁶A's and a stop codon. These A or m⁶A mRNAs were used for *in vitro* translation. No emetine was added until the end of the reaction when it was stopped by adding 200 μM emetine. Ribosome footprints were then visualized as described above.

Disome quantification by sucrose gradient fractionation

Disome quantification was performed as previously described.⁵¹ Cell lysate was prepared from MEFs using lysis buffer [20 mM Tris-HCl, pH 7.4, 150 mM KCl, 15 mM MgCl₂, 1% Triton-X, 1 mM DTT, and 1x EDTA-free protease inhibitor cocktail (ThermoFisher, 1861279)]. The lysate was passed through a 25G needle for 5 times and subjected to centrifugation at 12,000 × g for 10 min at 4°C to remove the nuclei. The lysate was quantified using NanoDrop (ThermoFisher). 2.6 μg/mL RNaseA was added to 200 μg lysate prepared in 400 μL and the reaction was incubated for 15 min at room temperature. The digestion reaction was quenched by adding 400 U SUPERase-In (ThermoFisher, AM2696). Digested lysate was subjected to 10-35% sucrose gradient centrifugation at 32,000 rpm for 2 h at 4°C on a SW 41 Ti rotor in a Beckman L-80 ultracentrifuge. The gradient was analyzed using a BioComp piston fractionator based on absorbance at 254 nm.

Visualization of ribosomal subunits identified in YTHDF interactome study on a collided disome

Cryo-EM structure of a collided disome⁵⁰ was retrieved from Protein Data Bank (<https://www.rcsb.org/>) using accession numbers 6HCM and 6HCQ. The fold change of signal intensity for each ribosome protein based on the YTHDF-BioID normalized to the eGFP-BioID control was used to calculate the proximity level score. For each YTHDF dataset, the proximity levels for each ribosomal subunit were normalized as a fraction of the cumulative proximity levels of all ribosomal subunits. We then filtered ribosomal subunits that were detected in the BioID analysis of all three YTHDF proteins. The average of the normalized proximity levels among three YTHDF proteins was used to color code ribosomal subunits on the structure of the collided disome using PyMOL.

Gene Ontology analysis

A list of genes was generated by filtering for m⁶A levels and for the increase in mRNA half-life in *Mettl3* knockout MEFs. These genes are considered m⁶A-regulated mRNAs (Table S6). m⁶A levels was quantified by summing the m⁶A stoichiometry of each m⁶A site on each mRNA based on a previous GLORI dataset.³⁷ Genes with above-median m⁶A levels among all m⁶A genes were designated highly methylated genes. For those genes, mRNA half-life was measured using TimeLapse-seq. Genes with the fold increase of mRNA half-life above 1 in *Mettl3* knockout MEFs relative to wild-type MEFs were selected as the input. Gene overrepresentation analysis among Gene Ontology was performed using enrichGO function using clusterProfiler 4.8.1^{105,106} on R v4.3.0.

QUANTIFICATION AND STATISTICAL ANALYSIS

Statistical analysis for each experiment can be found in the figures and figure legends, including the statistical tests used, sample size, definition of center, dispersion and precision measures, and definition of significance. Details of statistical analysis and software used are described in [STAR Methods](#) and [key resources table](#), including the statistical methods used to determine strategies for randomization and stratification and inclusion and exclusion of any data or subjects.

Supplemental figures

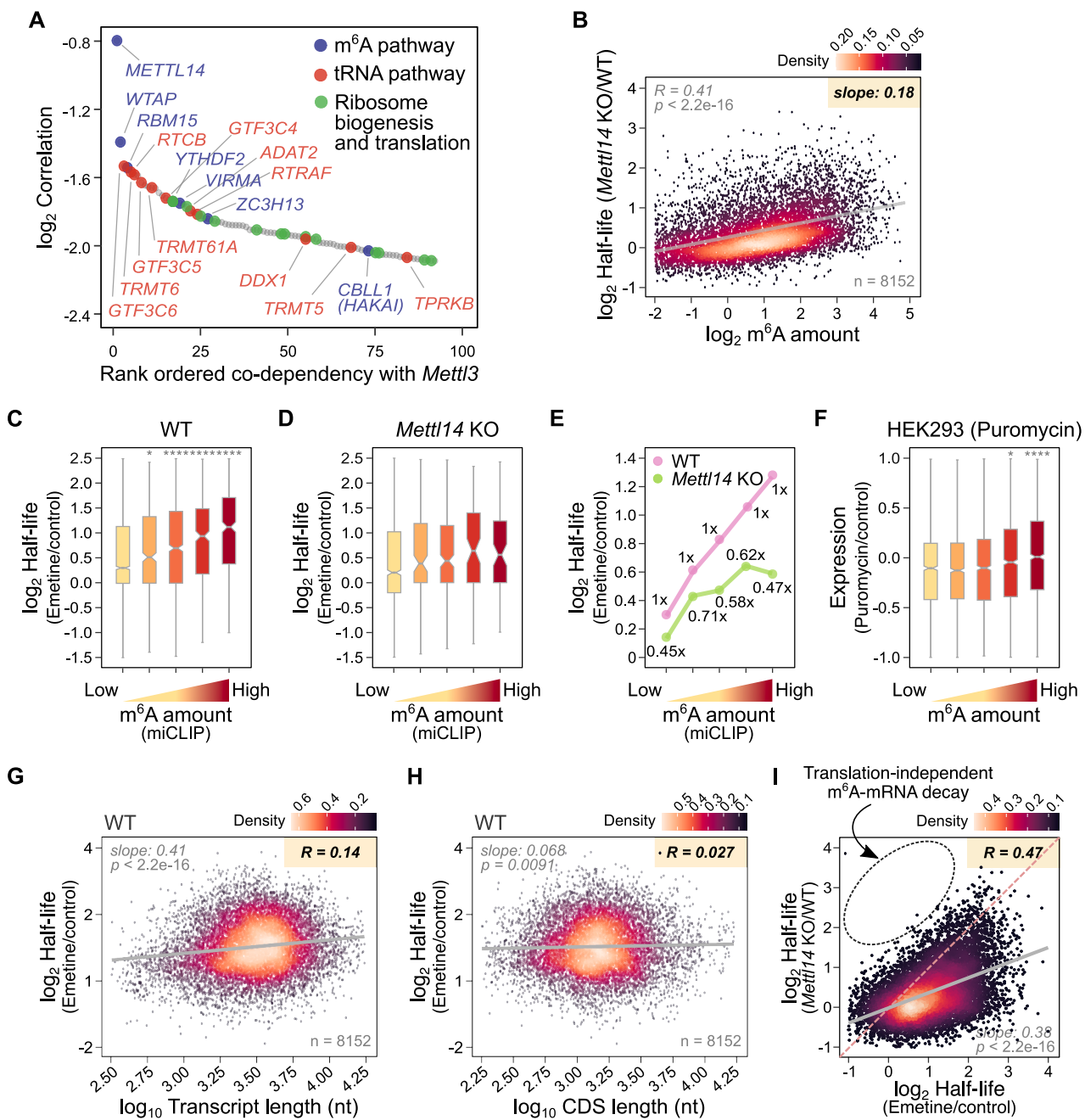


Figure S1. m⁶A-mRNA degradation is a translation-dependent process, related to Figure 1

(A) DepMap co-dependency analysis suggests a mechanistic link between the m⁶A pathway and translation. DepMap uses CRISPR-Cas9 to systematically disrupt nearly all genes (17,931 genes) and measure dependency scores (i.e., cellular growth rate in the absence of the gene) for each gene in >1,000 cell lines. A cell growth dependency score is calculated for each gene in each cell line. Any two genes that show similar dependency scores across all cell lines are often mechanistically linked.¹¹⁷ To find additional regulators of m⁶A-mRNA degradation, we selected the m⁶A methyltransferase *METTL3* and looked for genes with similar dependency scores. As expected, the other components of the m⁶A writer complex, i.e., *METTL14*, *RBM15*, *VIRMA*, *ZC3H13*, *HAKAI*, and *WTAP*, as well as the m⁶A effector protein *YTHDF2*, all appeared as genes that show similar dependency scores as *METTL3*. However, 30 genes involved in mRNA translation

(legend continued on next page)

were also among the top 100 genes that show the most similar dependency scores across cell lines with *Mettl3* knockout. These data suggest a link between the process of m⁶A-mediated mRNA degradation and translation.

(B) m⁶A promotes mRNA degradation. To confirm the degradation effect of m⁶A in our dataset, we measured mRNA half-life in *Mettl14* knockout mESC relative to wild-type cells. The cumulative m⁶A levels for each mRNA were determined by GLORI.³⁷ For mRNA, we plotted the change in half-life. As expected, highly methylated mRNAs show increased half-life in *Mettl14* knockout cells relative to lowly methylated mRNAs, and this change was in general in proportion to m⁶A levels. *R*, Pearson correlation coefficient; *p*, *p* value.

(C) Emetine stabilizes m⁶A-containing mRNA. Shown is an analysis of the change in mRNA half-life after emetine treatment determined using transcription inhibitor actinomycin D (10 µg/mL, 3 h). In this plot, the m⁶A level in each transcript was quantified using miCLIP,⁹¹ an antibody-based single-nucleotide resolution m⁶A mapping method, rather than GLORI.³⁷ mRNA half-life was measured in the absence and presence of emetine in mESC. mRNAs were grouped based on their m⁶A counts determined by miCLIP. The change in mRNA half-life after translation inhibition relative to vehicle treatment is plotted. For lowly methylated genes, mRNA half-life slightly increased when translation was inhibited. Highly methylated genes showed much more mRNA stabilization with translation inhibition. The effect of emetine is therefore seen regardless of the methods used to measure mRNA half-lives or m⁶A levels. Two-sided Wilcoxon signed-rank test; **p* < 2e-04, ***p* < 2e-08, ****p* < 2e-12, *****p* < 2e-16. Boxplots show the median, upper/lower quartiles, and whiskers at 1.5× interquartile ranges.

(D) To test whether translation-dependent degradation of the m⁶A-containing mRNAs depends on the presence of m⁶A, the experiment in (C) was repeated using *Mettl14* knockout mESC. Emetine elicited a much less prominent stabilization effect for genes that are normally highly methylated in the wild-type cell. The stabilization effect of emetine was no longer correlated with the amount of m⁶A. Two-sided Wilcoxon signed-rank test; **p* < 2e-04, ***p* < 2e-08, ****p* < 2e-12, *****p* < 2e-16. Boxplots show the median, upper/lower quartiles, and whiskers at 1.5× interquartile ranges.

(E) Plot of the median change in mRNA half-life shown in (C) and (D). To help compare the change in mRNA stabilization in the *Mettl14* knockout mESC, the fold-increase in mRNA half-life after emetine treatment in wild-type cells (pink) is considered as “1X” and the fold-stabilization in *Mettl14* knockout (green) relative to wild-type cells is indicated above each green dot.

(F) Translation inhibition using puromycin stabilizes m⁶A-mRNAs. Puromycin is a mechanistically distinct translation inhibitor. We used a previously published dataset of puromycin treatment in HEK293 cells,⁴¹ to examine the role of translation in m⁶A-mRNA degradation. mRNAs were grouped in pentiles based on their cumulative m⁶A levels determined by GLORI.³⁷ For each group of genes, the change in mRNA expression was plotted. Although puromycin treatment was associated with reduced expression in all groups, highly methylated mRNAs showed higher expression relative to lowly methylated mRNAs. This change in expression levels were proportional to methylation levels. Two-sided Wilcoxon signed-rank test; **p* < 2e-04, ***p* < 2e-08, ****p* < 2e-12, *****p* < 2e-16. Boxplots show the median, upper/lower quartiles, and whiskers at 1.5× interquartile ranges.

(G) To determine the effect of transcript length in translation-mediated m⁶A-mRNA degradation, we plotted the stabilization effect of emetine versus transcript length for each mRNA. Transcript lengths were mildly correlated with the change in mRNA half-lives after emetine treatment. However, this correlation was much smaller compared with when the effect of emetine was plotted with m⁶A levels in Figure 1C. *R*, Pearson correlation coefficient; *p*, *p* value.

(H) Similar to Figure S1G, but testing the effect of CDS length rather than transcript length. CDS lengths showed no observable correlation with the change in mRNA half-lives after emetine treatment. *R*, Pearson correlation coefficient; *p*, *p* value.

(I) A majority of m⁶A-mediated mRNA degradation requires active translation. The effect of m⁶A on mRNA stability was defined as the fold change in mRNA half-life in *Mettl14* knockout mESC compared with mRNA half-life in wild-type mESC. The effect of emetine on mRNA stability was defined as the fold change in mRNA half-life after emetine treatment to the control treatment in wild-type mESC. *n* = 11,239. *R*, Pearson correlation coefficient; *p*, *p* value.

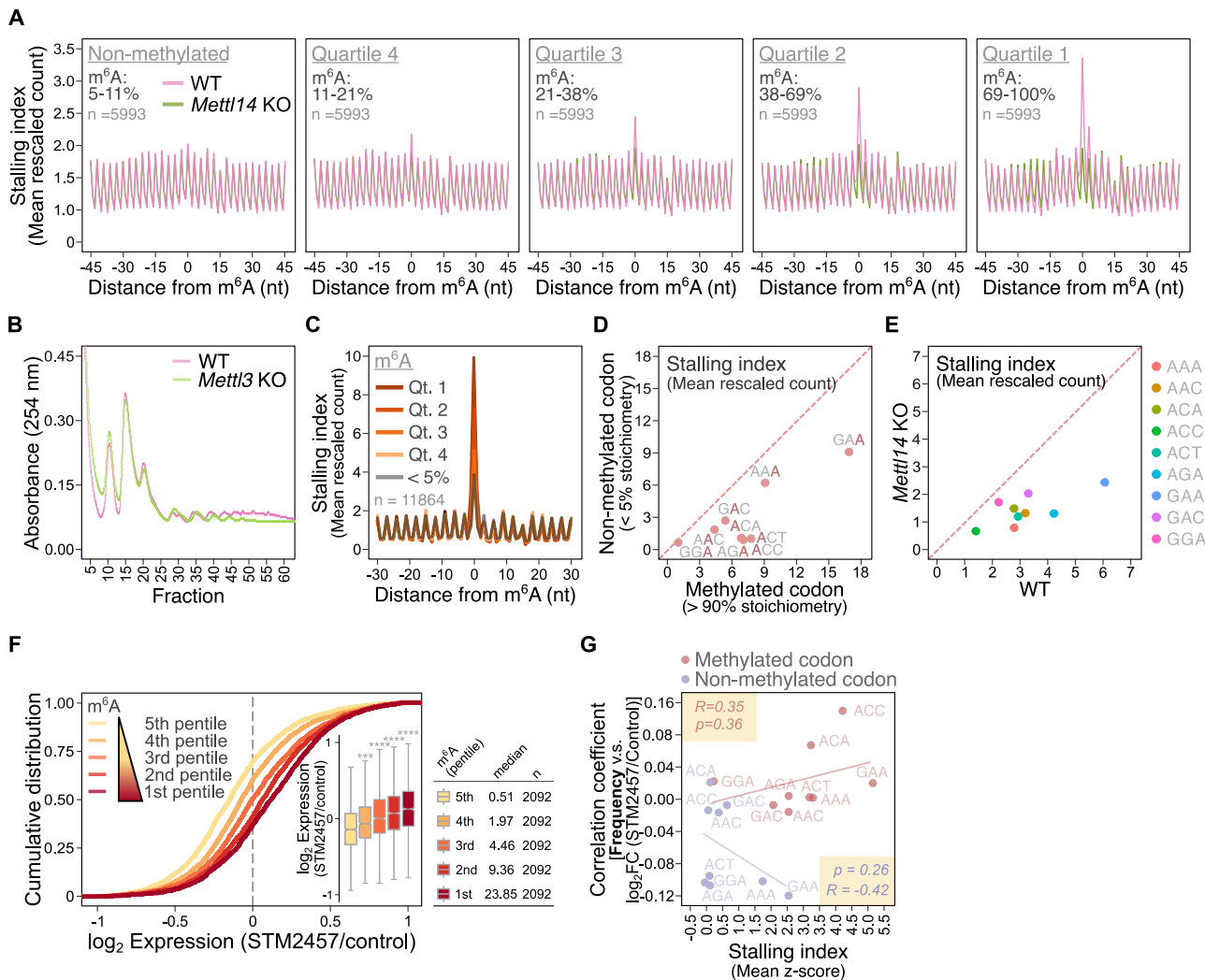


Figure S2. m⁶A-induced ribosome stalling is linked to m⁶A-mRNA degradation, related to Figure 2

(A) Ribosome stalling at m⁶A site is due to m⁶A. CDS m⁶A was grouped in pentiles based on m⁶A stoichiometry determined by GLORI.³⁷ For each group of CDS m⁶A, we plotted the mean rescaled A-site count relative to the first nucleotide of m⁶A-containing codons in wild-type and Mettl14 knockout mESC. Similar to HEK293T cells shown in Figure 3A, we saw a profound amount of stalled ribosomes at m⁶A sites with the degree of stalling in proportion to m⁶A stoichiometry. However, the ribosome stalling at the same sites were no longer observable in Mettl14 knockout mESC. These results suggest that pronounced ribosome stalls at m⁶A is due to the presence of m⁶A, rather than an inherent stalling propensity of m⁶A consensus sequences.

(B) Polysome profiles of lysates from wild-type and Mettl3 knockout MEFs.

(C) A-site quantification using mean rescaled counts. A-site of ribosomes were quantified as in Figure 3A, but using mean rescaled counts instead of Z score normalization. To determine stalling index, m⁶A sites that have ≥ 10 A-site counts within ± 30 nucleotide window was filtered for further analysis. A-site count was calculated for each nucleotide position within the window for each m⁶A site and was normalized by the mean A-site counts of all nucleotide positions within the same window. Stalling index was calculated as the mean of rescaled A-site count at each nucleotide position within the window for all m⁶A sites of interest. The overall effect is very similar to Figure 3A.

(D) Comparison of ribosome stalling at highly methylated m⁶A codons ($> 90\%$ stoichiometry) and non-methylated control codons ($< 5\%$ stoichiometry) using mean rescaled counts instead of mean Z score as in Figure 2B.

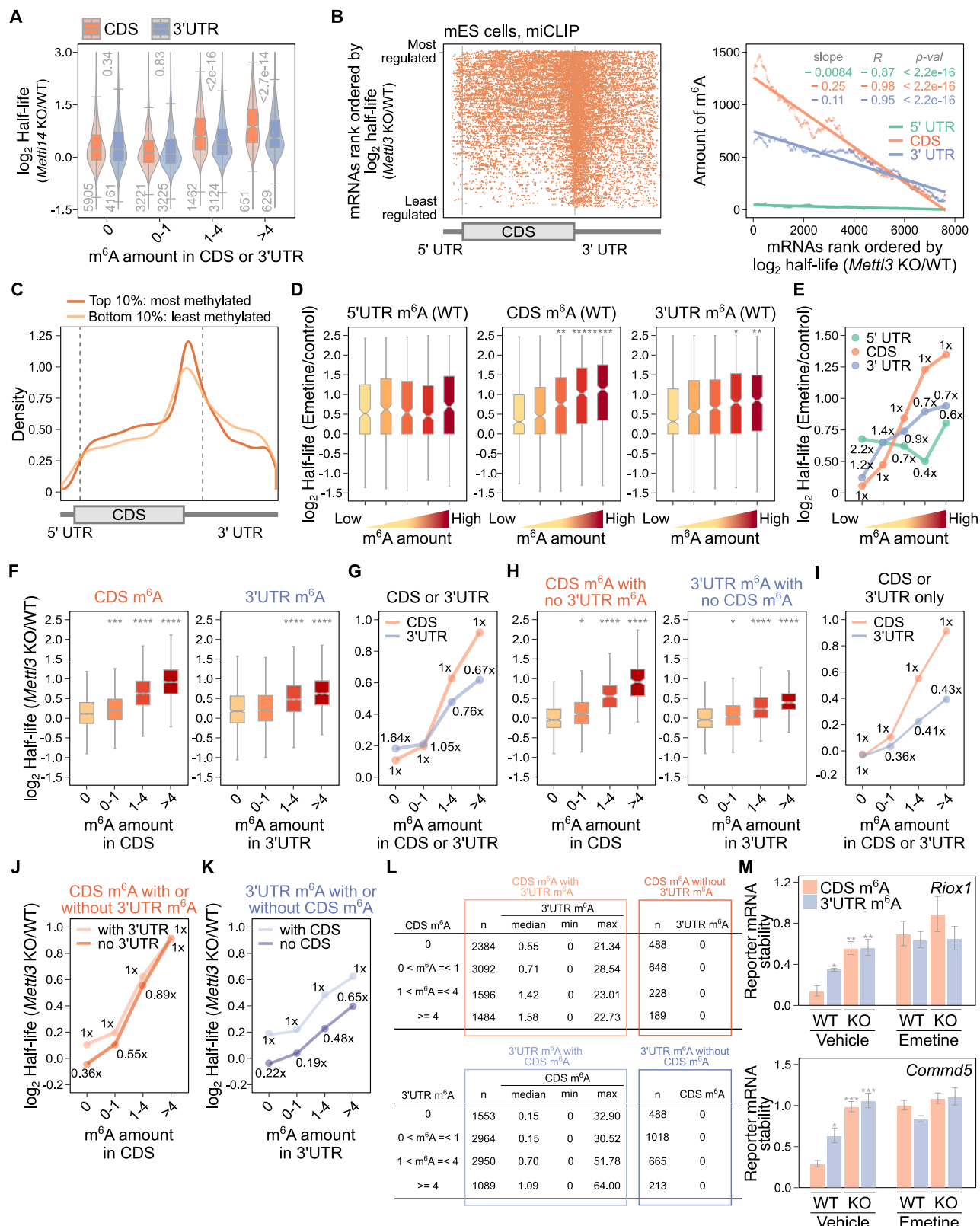
(E) Comparison of ribosome stalling at m⁶A-containing codons, and the same nucleotide position in Mettl14 mESC. The stalling index for the first nucleotide of each m⁶A-containing codon was calculated at codons that contain high-stoichiometry m⁶A ($> 75\%$ stoichiometry) in wild-type mESC. To test whether ribosome stalling at m⁶A site is induced by m⁶A, the stalling index for each codon at the same transcriptomic positions was also calculated in Mettl14 knockout mESC. Some codons such as GGA and GAC exhibit basal levels of stalling evident in Mettl14 knockout mESC. However, for every codon, stalling was substantially reduced in Mettl14 knockout mESC compared with wild-type mESC, indicating that m⁶A induces ribosome stalling. The stalling index for several m⁶A-containing codons is different in mESC and in HEK293T cells. The stalling index at each codon is likely influenced by the abundance of the corresponding aminoacyl-tRNA in each cell type.

(F) METTL3 inhibitor STM2457 stabilizes m⁶A-mRNAs. To confirm the effect of METTL3 inhibitor STM2457 on m⁶A-mRNA stabilization, we first grouped transcripts into pentiles based on m⁶A levels. Shown are cumulative distribution plots of the fold change in mRNA expression after STM2457 treatment (20 μ M, 24 h) relative to the vehicle treatment in HEK293T cells. STM2457 increased the expression of m⁶A-mRNA, and this effect was proportional to methylation levels. Insets

(legend continued on next page)

show boxplots of mRNA stabilization for each group of mRNAs. mRNA expression data are taken from GSE203642.⁴⁷ Two-sided Wilcoxon signed-rank test; * $p < 2e-04$, ** $p < 2e-08$, *** $p < 2e-12$, **** $p < 2e-16$. Boxplots show the median, upper/lower quartiles, and whiskers at 1.5× interquartile ranges.

(G) Similar analysis as in [Figure 2D](#). In this analysis, the fraction of non-methylated codons to the total number of codons in the respective CDS was first calculated. For each codon, the correlation coefficient between the fraction and the destabilization effect of m⁶A was then plotted in purple. Correlation for corresponding plots for methylated codons is shown in red. As seen using absolute number of non-methylated codon ([Figure 2D](#)), the fraction of non-methylated codons showed an anti-correlation with the destabilization effect of m⁶A (see y axis). Additionally, the correlation coefficients between the fraction of codons and the destabilization effect of m⁶A showed a slight anti-correlation (see x axis vs. y axis). Pearson correlation.



(legend on next page)

Figure S3. m⁶A sites that encounter the ribosome induce degradation, related to Figure 2

(A) To test the role of m⁶A-induced ribosome stalling, we asked whether m⁶A sites in the 3' UTR contribute to m⁶A-mediated mRNA degradation. Similar to Figure 2F, but in mESC, we compared the m⁶A-mediated mRNA degradation effect based on the levels m⁶A in the CDS or 3' UTR for each mRNA measured by GLORI.³⁷ m⁶A-mediated mRNA degradation was calculated by comparing the mRNA half-life in wild-type mESCs with *Mettl14* knockout mESC. As seen in Figure 2F, the amount of CDS m⁶A was more strongly correlated to m⁶A-mediated mRNA degradation compared with the amount of 3' UTR m⁶A. Top, *p* values; bottom, *n* = number of transcripts in each group of mRNAs. Two-sided Wilcoxon signed-rank test. Boxplots show the median, upper/lower quartiles, and whiskers at 1.5× interquartile ranges.

(B) The potential of ribosome to encounter m⁶A correlates with m⁶A-mRNA instability. (Left) Similar to Figure 2H, but mRNA half-lives were measured based on an actinomycin D and m⁶A sites were quantified based on miCLIP.⁹¹ Genes were ranked on the y axis based on their fold-increase in mRNA half-life in *Mettl3* knockout (*Mettl3* KO) mESC relative to wild-type (WT) mESC. An increase in mRNA half-life in *Mettl3* knockout reflects the presence of destabilizing m⁶A sites. The length of 5' UTR, CDS, and 3' UTR of all mRNAs were scaled so that each region was the same length in all mRNAs. The location of m⁶A along each transcript was plotted. mRNAs with the largest increase in half-life in *Mettl3* knockout (i.e., mRNAs most regulated by m⁶A) show m⁶A all along the CDS and 3'UTR. However, in mRNAs least stabilized by *Mettl3* knockout (i.e., mRNAs least regulated by m⁶A), m⁶A was nearly absent in CDS while still abundant in 3' UTR. These data suggest that CDS m⁶A promote m⁶A-dependent degradation to a larger degree than 3' UTR m⁶A. (Right) Quantification of m⁶A on the left. m⁶A levels were quantified in the 5' UTR, CDS, and 3' UTR by summing the m⁶A stoichiometries of each mapped m⁶A site. A sliding window measuring 500 transcripts was used to plot m⁶A levels from the most stabilized transcripts by *Mettl3* knockout to least stabilized transcripts. The CDS m⁶A levels were more strongly correlated with mRNA degradation, compared with 5' UTR and 3' UTR m⁶A levels. *R*, Pearson correlation coefficient; *p*, *p* value.

(C) Shown is a m⁶A metagene plot for the top 10% most and least methylated m⁶A-mRNAs measured by GLORI.³⁷ The amount of m⁶A in the CDS is slightly higher on the most methylated m⁶A-mRNA, while the amount of 3' UTR m⁶A is slightly higher on the least methylated m⁶A-mRNA. This suggests that highly methylated mRNAs tend to have slightly more m⁶A in the CDS. These mRNAs are therefore more prone to translation-dependent mRNA degradation.

(D) Translation-dependent m⁶A-mRNA degradation is mediated by m⁶A that encounters the ribosome. To test whether the effect of CDS m⁶A is due to the ability of the ribosome to encounter these m⁶A sites, we first grouped m⁶A-mRNAs based on the amount of m⁶A in 5' UTR, CDS, and 3' UTR in MEFs based on GLORI.³⁷ We then measured the fold change in mRNA half-life induced by emetine in MEFs for each group of m⁶A-mRNA. The amount of CDS m⁶A most strongly correlated with stabilizing effect of emetine. However, the stabilizing effect of 3' UTR m⁶A was much lower. These data suggest that CDS m⁶A more effectively drives m⁶A-mRNA degradation because they are the only m⁶A that encounters the ribosome. Boxplots show the median, upper/lower quartiles, and whiskers at 1.5× interquartile ranges.

(E) Plot of the median change in mRNA half-life shown in (D). We defined the fold-increase in mRNA half-life as 1× for CDS m⁶A (pink) for each group of mRNAs. The fractional reduction in mRNA half-life increase is shown for each 5' UTR (green) and 3' UTR (blue) m⁶A group.

(F) m⁶A sites that encounter the ribosome are more strongly correlated with m⁶A-mediated mRNA degradation. To test the correlation between CDS or 3' UTR m⁶A and m⁶A-mediated mRNA degradation, we quantified cumulative m⁶A levels in the CDS of mRNAs, or 3' UTR of mRNAs in MEFs, by summing the m⁶A stoichiometries in these regions. We then grouped transcripts based on their CDS or 3' UTR m⁶A levels. The fold change in mRNA half-life in *Mettl3* knockout MEFs relative to wild-type MEFs was measured for each group of genes. Although m⁶A levels in both CDS and 3' UTR correlated with the increased half-life by m⁶A depletion, CDS m⁶A levels has stronger correlation. Two-sided Wilcoxon signed-rank test; **p* < 2e−04, ***p* < 2e−08, ****p* < 2e−12, *****p* < 2e−16. Boxplots show the median, upper/lower quartiles, and whiskers at 1.5× interquartile ranges.

(G) Plot of the median change in mRNA half-life shown in (F). We defined the fold-increase in mRNA half-life as 1× for CDS m⁶A for each group of mRNAs. The fractional reduction in mRNA half-life increase is shown for each 3' UTR m⁶A group.

(H) To dissociate the effect of CDS m⁶A from 3' UTR m⁶A and vice versa, we selected mRNAs that have m⁶A only in either the CDS or the 3' UTR. We then quantified the cumulative CDS and 3'UTR m⁶A levels for each mRNA. We then grouped transcripts based on their CDS or 3' UTR m⁶A levels. The fold change in mRNA half-life in *Mettl3* knockout MEFs relative to wild-type MEFs was measured for each group of genes. Although m⁶A levels in both CDS and 3' UTR correlated with the increased half-life, CDS m⁶A levels has stronger correlation. The stabilizing effect of 3' UTR m⁶A was much lower. Notice that the effect of 3' UTR m⁶A is lower than what was observed in (F), which suggests that some of the degradation effect for 3' UTR m⁶A seen in (F) comes from co-occurring CDS m⁶A in these mRNAs. Two-sided Wilcoxon signed-rank test; **p* < 2e−04, ***p* < 2e−08, ****p* < 2e−12, *****p* < 2e−16. Boxplots show the median, upper/lower quartiles, and whiskers at 1.5× interquartile ranges.

(I) Plot of the median change in mRNA half-life shown in (H). Comparison of this plot with (G) shows that the effect of 3' UTR m⁶A in (G) was driven in part by co-occurring m⁶A from the CDS.

(J) 3' UTR m⁶A does not substantially enhance the degradation effect of CDS m⁶A. To measure the effect of 3' UTR m⁶A on mRNA half-life, we compared transcripts with the same CDS m⁶A levels but lacking or containing 3' UTR m⁶A. mRNAs were grouped based on the cumulative CDS m⁶A levels measured by GLORI,³⁷ and their increase in mRNA half-life in m⁶A-deficient MEFs (*Mettl3* knockout) was plotted. The presence of 3' UTR m⁶A did not substantially increase the degradation effect of CDS m⁶A.

(K) Similar analysis as in (J), but mRNAs were grouped based on the 3' UTR m⁶A levels for mRNAs with or without CDS m⁶A. The presence of CDS m⁶A substantially increased the degree of m⁶A-mediated degradation, as measured by the increase in mRNA half-life in *Mettl3* knockout MEFs. This suggests that the effects seen with 3' UTR m⁶A are due, in part, to co-occurring CDS m⁶A.

(L) Tables showing the amount of 3' UTR m⁶A for each group of CDS m⁶A (top) and the amount of CDS m⁶A for each group of 3' UTR m⁶A (bottom) in (J) and (K).

(M) To test the importance of the ability of ribosome to encounter m⁶A for mRNA degradation, we created reporters derived from endogenous transcripts (*Riox1* and *Commd5*) that are highly methylated in the coding sequence and destabilized by m⁶A. The reporters contained mutations that served as primer amplifications sites to allow RT-qPCR amplification of the reporter mRNA, and not the endogenous transcript. All of the m⁶A consensus sites (DRACH,^{45,46} where D = A,G,U; R = A,G, H = A,C,U) were located in the CDS and were thus designated CDS m⁶A reporters. To create the 3' UTR m⁶A reporters, we introduced a stop codon before the first DRACH sequence in the CDS, which converts CDS m⁶A sites into 3' UTR m⁶A sites. We measured the stability of the CDS and 3'UTR m⁶A reporter mRNAs in WT and *Mettl14* knockout (KO) mESC. The CDS m⁶A reporter was significantly less stable than the 3' UTR reporter in wild-type cells. However, in *Mettl14* knockout mESC, the CDS m⁶A reporter and 3' UTR m⁶A reporter mRNA had similar stability. To test whether the ability of the ribosome to encounter CDS m⁶A is important for the destabilization effect of CDS m⁶A, we measured the stability of the reporter mRNAs after emetine treatment (200 μM, 3 h). The CDS m⁶A reporters were stabilized after emetine treatment in WT mESC. However, the stabilization effect of emetine was smaller in *Mettl14* knockout mESC. Together, these results suggest that the ability of the ribosome to encounter CDS m⁶A is critical for m⁶A-mediated mRNA degradation.

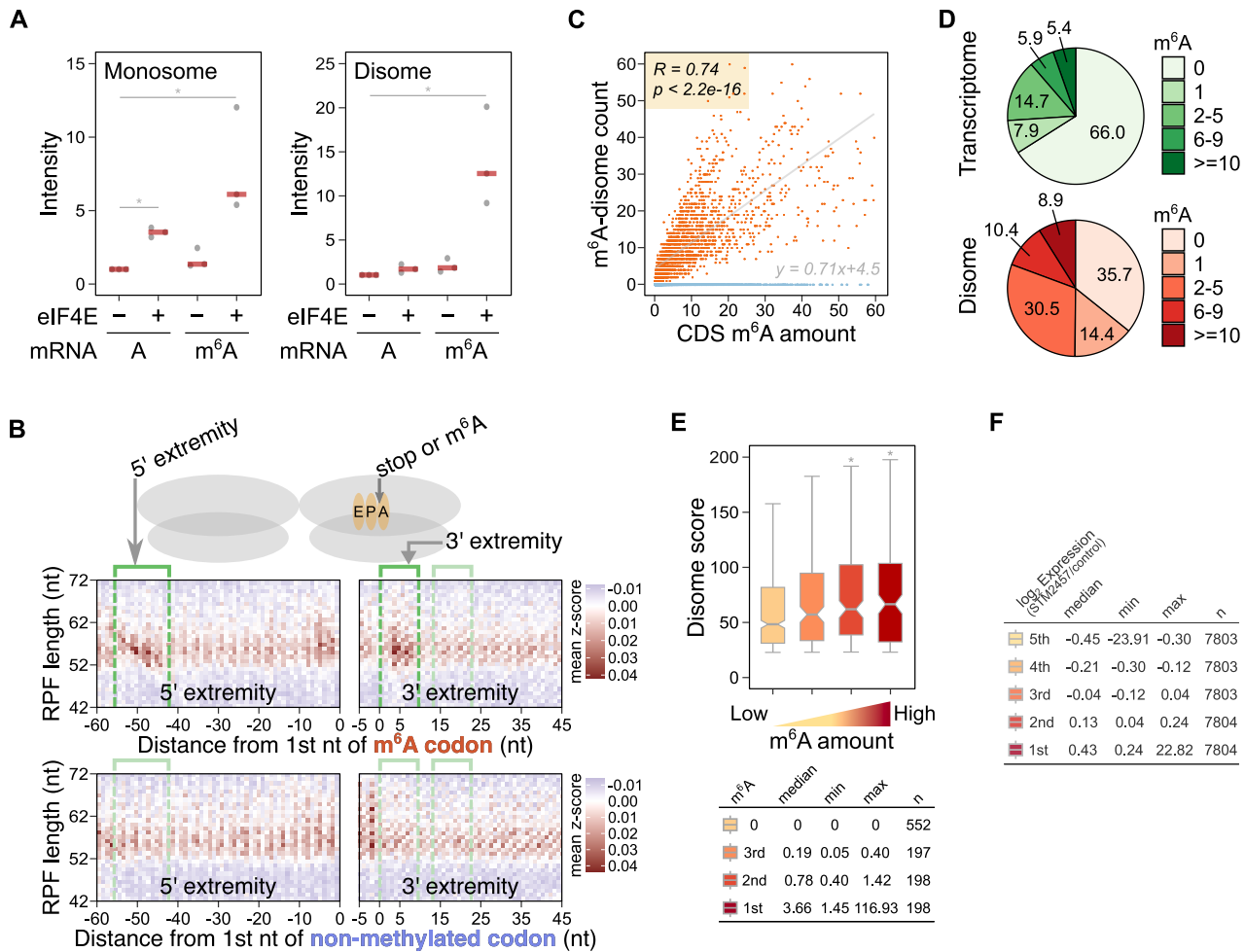


Figure S4. m⁶A induces ribosome collisions, related to Figure 3

- (A) Quantification of monosome and disome footprints in the *in vitro* ribosome footprint assay in Figure 3A. The signal intensity was normalized to non-methylated transcript without elF4E for each type of footprints. $n = 3$.
- (B) Raw Z scores of disome footprints surrounding m⁶A-containing codons shown in Figure 3B. This image uses the same data as presented in Figure 3B, except it is not background-subtracted using footprints collected at non-methylated control codon sequences. Background was calculated as disome footprints around non-methylated sequence-matched control codons. A potential explanation for the enrichment at the 5' and 3' extremities of m⁶A codons seen in Figure 3B is that the 5' and 3' extremities are instead depleted at non-methylated codons. To address this possibility, we plotted the raw Z scores of disome footprints surrounding m⁶A-containing codons and control non-methylated codons separately. As shown in Figure 3B, disome footprints at m⁶A sites exhibit a 5' extremity ~44–48 nucleotides upstream of the m⁶A-containing A-site, corresponding to the lagging collided ribosome in a true disome, while the leading stalled ribosome exhibits a 3' extremity only 4–8 nucleotides downstream of the m⁶A codon. In contrast, disome footprints were not enriched at these nucleotide positions at non-methylated control codons. In addition, in disome footprints at the stop codon in Figure 3B, we found "sub-disomes." Sub-disomes have previously been described in yeast when ribosomes were stalled at histidine codons after the knockdown of *histidyl-tRNA synthetase 1*.⁴⁴ These smaller fragments were suggested to represent disome intermediates that are undergoing disassembly of the collided ribosome.⁴⁴ The 3' extremity of sub-disome footprints were located 14–21 nt downstream of the stop codon, similarly to true disomes. However, the 5' extremity of sub-disomes were broadly distributed at 23–42 nt upstream of the stop codon.
- (C) The amount of m⁶A-induced collided ribosomes correlates with the amount of CDS m⁶A. For each of m⁶A, a collided disome footprints whose the 5' and 3' extremities are located at 44–54 nt upstream and 4–8 nt downstream of the first nucleotide of the m⁶A-containing codon, respectively, was counted as a disome associated with the respective m⁶A. For this analysis, CDS m⁶A located less than 120 nt from either the start and stop codons was excluded to avoid stalled ribosomes at start and stop codons. For each transcript ($n = 10,736$), the cumulative amount of m⁶A-associated disomes was computed. The amount of m⁶A-associated disomes was plotted against the amount of CDS m⁶A for each transcript. Pearson correlation.
- (D) Collided disomes are abundant on m⁶A-containing mRNAs. Here, we used a previous map of disomes on mRNAs.⁵² We asked whether disomes are enriched on m⁶A-containing mRNA. Based on miCLIP, ~33% of all expressed mRNAs had at least one m⁶A. However, among mRNAs that contained a mapped collided ribosomes, ~64% of collided ribosomes-containing mRNAs had at least one m⁶A. Overall, disome-containing mRNAs were more likely to have one or more m⁶A sites compared with all expressed mRNAs.
- (E) The amount of disomes increases in proportion to the amount of CDS m⁶A. The amount of disomes per mRNA was plotted for each group for mRNAs grouped based on the cumulative amount of CDS m⁶A determined by GLORI. mRNAs with high CDS m⁶A levels had more disomes compared with mRNAs with low CDS

(legend continued on next page)

m^6A , and this effect was proportional to the amount of CDS m^6A , supporting the idea that CDS m^6A promotes ribosome collision. Boxplots show the median, upper/lower quartiles, and whiskers at $1.5 \times$ interquartile ranges.

(F) The number of transcripts and their median fold change in expression after STM2547 treatment relative to the control for each group of transcripts shown in [Figure 3E](#).

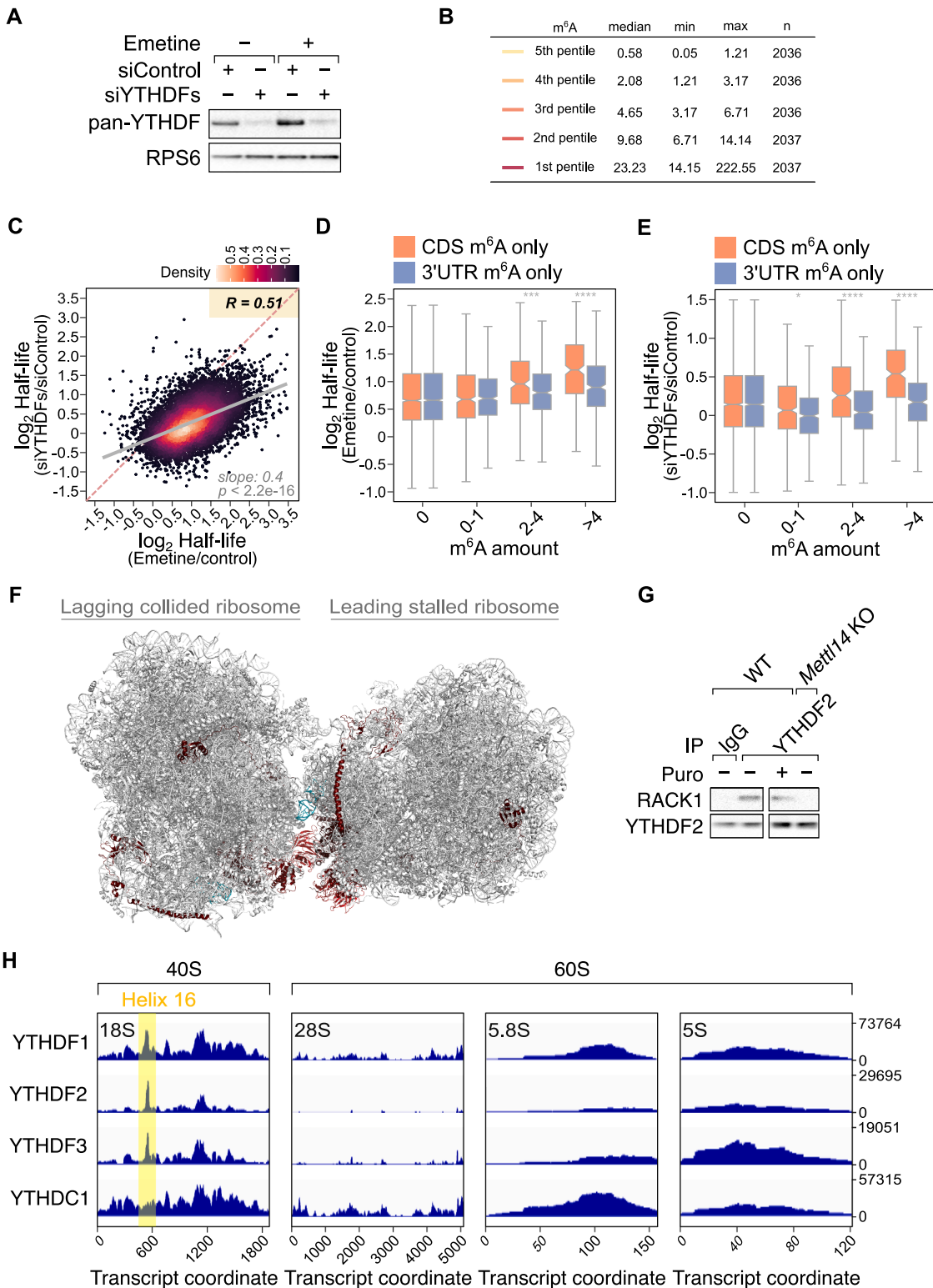


Figure S5. m⁶A-induced ribosome collisions promote YTHDF protein binding for m⁶A-mRNA degradation, related to Figure 4

(A) Western blotting showing efficiency of YTHDF triple knockdown in HeLa cells. YTHDF proteins were depleted in HeLa cells by siRNA-mediated triple knockdown using siRNA targeting each YTHDF paralog (siYTHDFs). Non-targeting siRNA was used as the control.

(B) The number of transcripts and their minimum, median, and maximum methylation levels for each group of transcripts shown in Figure 4A.

(legend continued on next page)

(C) mRNA stabilization by emetine correlates with mRNA stabilization seen with YTHDF1-3 depletion. mRNA half-life was measured in *YTHDF1-3* triple knockdown HeLa cells and compared with mRNA half-life in control siRNA-treated HeLa cells. The effect of emetine on mRNA stability was defined as the fold change in mRNA half-life after emetine treatment compared with vehicle-treated HeLa cells. In this plot, we see only a small number of mRNAs that may be degraded by YTHDF proteins and independent of translation. The effects of YTHDF depletion and emetine generally correlate, suggesting that YTHDF-mediated mRNA degradation is part of the overall translation-mediated m⁶A-mRNA degradation pathway. Pearson correlation.

(D) CDS m⁶A is more strongly linked to translation-mediated mRNA degradation. mRNAs were filtered for transcripts that have m⁶A only in their CDS or only in their 3' UTR. mRNAs were then grouped based on the amount of m⁶A in CDS for mRNAs with only CDS m⁶A or in 3' UTR for mRNAs with only 3' UTR m⁶A. For each group of mRNAs, the effect of emetine on mRNA stability was defined as the fold change in mRNA half-life after emetine treatment relative to the control treatment in HeLa cells. The effect of emetine is more strongly correlated to the amount of CDS m⁶A, compared with 3' UTR m⁶A. Two-sided Wilcoxon signed-rank test; **p* < 2e-04, ***p* < 2e-08, ****p* < 2e-12, *****p* < 2e-16. Boxplots show the median, upper/lower quartiles, and whiskers at 1.5× interquartile ranges.

(E) CDS m⁶A is more strongly linked to YTHDF-mediated mRNA degradation. mRNAs were filtered and grouped as described in (D). For each group of mRNAs, the effect of YTHDF proteins on mRNA stability was defined as the fold change in mRNA half-life in *YTHDF* triple knockdown HeLa cells relative to mRNA half-life in control knockdown HeLa cells. The effect of YTHDF proteins is correlated to the amount of CDS m⁶A, but not 3' UTR m⁶A. Two-sided Wilcoxon signed-rank test; **p* < 2e-04, ***p* < 2e-08, ****p* < 2e-12, *****p* < 2e-16. Boxplots show the median, upper/lower quartiles, and whiskers at 1.5× interquartile ranges.

(F) Ribosomal subunits identified in a YTHDF protein interactome study⁵⁸ are labeled in a collided disome cryo-EM structure.⁵⁰ The normalized proximity level of each ribosomal subunit relative to the eGFP control for each YTHDF protein was averaged and used to color code each protein. Shown here is the back side of the collided disome shown in Figure 4D. No cluster of ribosomal subunits with high levels of YTHDF protein proximity was observed outside of the collided ribosome interface.

(G) The interaction of YTHDF2 with RACK1 depends on translation and m⁶A. To understand how YTHDF2 binds to RACK1, YTHDF2 was immunoprecipitated from RNaseA-treated mESC lysates, and the coprecipitated RACK1 levels was measured by western blotting. RACK1 was readily detected in YTHDF2 immunoprecipitates under the control condition in WT mESC. However, this interaction was substantially reduced after puromycin treatment (100 µg/mL, 1 h), suggesting that translation or the 80S structure promotes the YTHDF2-RACK1 interaction. In addition, RACK1 was markedly reduced in YTHDF2 immunoprecipitates from *Mettl14* knockout cells. Blot image was separated after imaging to remove the irrelevant lanes between the shown lanes. These data support a model where translating ribosomes may need to encounter m⁶A to induce the YTHDF2-RACK1 interaction.

(H) YTHDF iCLIP shows YTHDF protein interaction with helix 16 of 18S rRNA in the 40S ribosomal subunit. YTHDF1, YTHDF2, and YTHDF3 iCLIP signal over 18S, 28S, 5.8S, and 5S rRNA was visualized. A common interaction site helix 16 on 18S was highlighted in yellow. As a control, the iCLIP signal of the nuclear-localized m⁶A reader YTHDC1 was also shown.

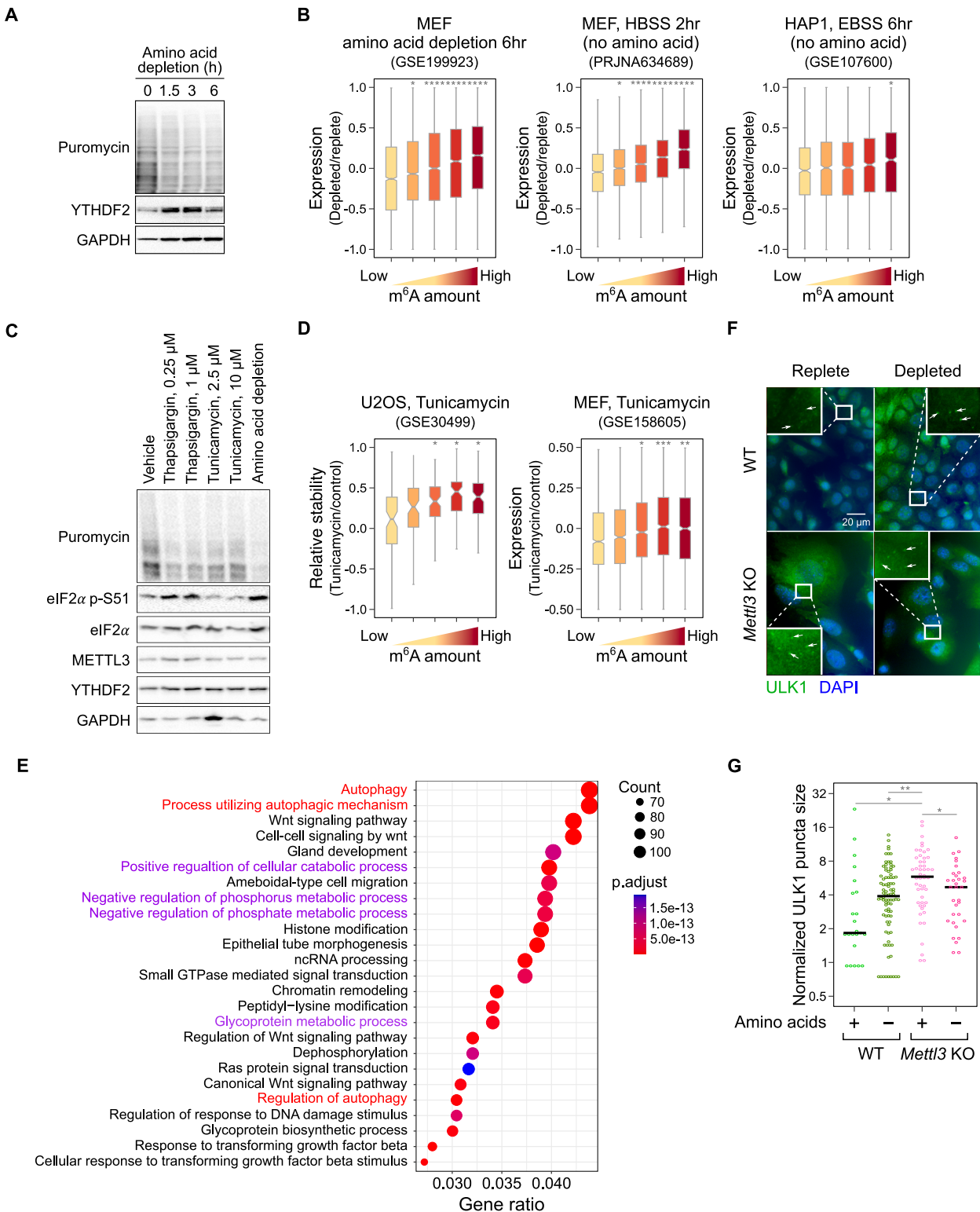


Figure S6. Cellular stresses stabilize m⁶A-mRNAs, related to Figure 5

(A) YTHDF2 expression is not reduced following amino acid depletion. We considered the possibility that the impaired m⁶A-mRNA degradation after amino acid depletion was due to reduced YTHDF2 levels. However, western blotting showing no detectable decrease in YTHDF2.

(legend continued on next page)

(B) Nutrient depletion stabilizes m⁶A-mRNAs based on reanalysis of previously published datasets. To test whether nutrient depletion stabilizes m⁶A-mRNA in other independent datasets, we repeated the analysis shown in Figure 5C in previously published RNA sequencing (RNA-seq) datasets of amino-acid-depleted MEFs^{69,70} and HAP1¹¹⁸ cells. In the first two studies (GEO: GSE199923, left; ENA: PRJNA634689, middle), MEFs were cultured in amino acid depletion media (amino acid-free DMEM supplemented with 10% dialyzed fetal bovine serum [FBS]) for 6 h and Hank's balanced salt solution (HBSS) (an amino acid and serum-free buffer) for 2 h, respectively. In another study (GEO: GSE107600, right), HAP1 cells were subjected to Earle's balanced salt solution (EBSS) (an amino acid and serum-free buffer) for 6 h. For each dataset, we grouped mRNAs into pentiles based on their cumulative m⁶A levels. For each group of genes, we plotted the change in mRNA expression after nutrient depletion relative to the nutrient replete state. Highly methylated mRNAs showed increased expression, with the effect proportional to methylation levels. Two-sided Wilcoxon signed-rank test; * $p < 2e-04$, ** $p < 2e-08$, *** $p < 2e-12$, **** $p < 2e-16$. Boxplots show the median, upper/lower quartiles, and whiskers at 1.5× interquartile ranges.

(C) Tunicamycin and thapsigargin suppress translation. To measure the translation rate after cell stresses, we treated MEFs as indicated for 3 h, followed by 10 min puromycin treatment to label nascent protein synthesis (100 µg/mL). Amino acid depletion was performed by subjecting cells to the amino-acid-depleted media. Puromycin incorporation was detected by anti-puromycin immunoblotting. Amino acid depletion leads to the largest decrease in nascent protein synthesis, although the other stresses caused partial reduction in translation relative to control.

(D) Tunicamycin, an endoplasmic reticulum stress inducer, stabilizes m⁶A-mRNAs. To test whether other forms of cellular stress besides amino acid depletion stabilize m⁶A-mRNA, we examined gene expression after tunicamycin treatment. mRNAs were grouped into pentiles based on cumulative m⁶A levels. Shown are boxplots of the fold change in gene expression after tunicamycin treatment relative to the control treatment. For U2OS cells, we plotted the change in mRNA stability for each group of genes. mRNA stability was calculated using a linear regression model based on the expression levels throughout the time course of the tunicamycin treatment. In the case of MEFs, highly methylated mRNAs showed a larger increase in expression levels after tunicamycin treatment relative to lowly methylated mRNAs. Two-sided Wilcoxon signed-rank test; * $p < 2e-04$, ** $p < 2e-08$, *** $p < 2e-12$, **** $p < 2e-16$. Boxplots show the median, upper/lower quartiles, and whiskers at 1.5× interquartile ranges.

(E) Genes regulated by m⁶A are related to autophagy and metabolic processes. Gene Ontology analysis was performed on 2,567 genes that were identified based on their high methylation levels and the finding that they are stabilized in *Mettl3* knockout MEFs. We quantified m⁶A levels for each mRNA by summing the m⁶A stoichiometries for each m⁶A site for each mRNA. We defined highly methylated mRNA as those above the median m⁶A levels among m⁶A-mRNAs. Genes were defined as stabilized in *Mettl3* knockout cells if the fold-increase of mRNA half-life was >1 in *Mettl3* knockout cells compared with wild-type MEFs.

(F) m⁶A-depleted cells show elevated autophagy levels even in amino-acid-replete conditions. Amino acid depletion can induce various cellular pathways that promote autophagy and other adaptive responses to stress. To selectively examine the effect of m⁶A-mRNA stabilization, we examined *Mettl3* knockout MEFs for evidence of stress responses. In these experiments, we cultured *Mettl3* knockout MEFs in amino-acid-replete media, and immunostained *Mettl3* knockout MEFs using an antibody for ULK1, which label autophagosomes, and thus serves as an autophagy marker.¹¹⁹ Basal autophagy levels, as measured by ULK1 puncta, were minimal in wild-type cells cultured in amino-acid-replete media. ULK1 puncta were readily detected after amino acid depletion of wild-type MEFs (3 h). However, autophagy levels were elevated in *Mettl3* knockout MEFs, even in cells cultured in amino-acid-replete media. Amino acid depletion in *Mettl3* knockout MEFs showed no further increase in ULK1 puncta.

(G) Quantification of ULK1-labeled puncta size in (F). Size of each ULK1-labeled puncta was measured and normalized to the cell surface area. One-way ANOVA with Tukey multiple comparison test; * $p < 0.033$, ** $p < 0.0021$, *** $p < 0.00020$, **** $p < 0.00010$.